AFRL-RQ-WP-TR-2019-0183

TRANSITIONAL ZONE LENGTH AND SIMULATION OF DISCRETE ROUGHNESS FOR HYPERSONIC BOUNDARY LAYERS

Roger L. Kimmel, Matthew W. Tufts, and Nicholas J. Bisek

Hypersonic Sciences Branch
High Speed Systems Division

Thomas J. Juliano

The University of Notre Dame

Joseph S. Jewell

Purdue University

OCTOBER 2019
Final Report

DISTRIBUTION STATEMENT A. Approved for public release. Distribution is unlimited.

STINFO COPY

AIR FORCE RESEARCH LABORATORY
AEROSPACE SYSTEMS DIRECTORATE
WRIGHT-PATTERSON AIR FORCE BASE, OH 45433-7542
AIR FORCE MATERIEL COMMAND
UNITED STATES AIR FORCE

NOTICE AND SIGNATURE PAGE

Using Government drawings, specifications, or other data included in this document for any purpose other than Government procurement does not in any way obligate the U.S. Government. The fact that the Government formulated or supplied the drawings, specifications, or other data does not license the holder or any other person or corporation; or convey any rights or permission to manufacture, use, or sell any patented invention that may relate to them.

This report was cleared for public release by the USAF 88th Air Base Wing (88 ABW) Public Affairs Office (PAO) and is available to the general public, including foreign nationals.

Copies may be obtained from the Defense Technical Information Center (DTIC) (http://www.dtic.mil).

AFRL-RQ-WP-TR-2019-0183 has been reviewed and is approved for publication in accordance with assigned distribution statement.

This report is published in the interest of scientific and technical information exchange, and its publication does not constitute the Government's approval or disapproval of its ideas or findings.

REPORT DOCUMENTATION PAGE

Form Approved OMB No. 0704-0188

1. REPORT DATE *(DD-MM-YY)*	2. REPORT TYPE	3. DATES COVERED *(From - To)*
October 2019	Final	1 March 2015 – 31 October 2019

4. TITLE AND SUBTITLE
TRANSITIONAL ZONE LENGTH AND SIMULATION OF DISCRETE ROUGHNESS FOR HYPERSONIC BOUNDARY LAYERS

5a. CONTRACT NUMBER In-house
5b. GRANT NUMBER
5c. PROGRAM ELEMENT NUMBER 61102F

6. AUTHOR(S)
Roger L. Kimmel, Matthew W. Tufts, and Nicholas J. Bisek (AFRL/RQHF)
Thomas J. Juliano (The University of Notre Dame)
Joseph S. Jewell (Purdue University)

5d. PROJECT NUMBER 3002
5e. TASK NUMBER
5f. WORK UNIT NUMBER Q1FN

7. PERFORMING ORGANIZATION NAME(S) AND ADDRESS(ES)
Hypersonic Sciences Branch (AFRL/RQHF)
High Speed Systems Division
Air Force Research Laboratory Aerospace Systems Directorate
Wright-Patterson Air Force Base, OH 45433-7542
Air Force Materiel Command, United States Air Force

The University of Notre Dame

Purdue University

8. PERFORMING ORGANIZATION REPORT NUMBER
AFRL-RQ-WP-TR-2019-0183

9. SPONSORING/MONITORING AGENCY NAME(S) AND ADDRESS(ES)
Air Force Research Laboratory
Aerospace Systems Directorate
Wright-Patterson Air Force Base, OH 45433-7542
Air Force Materiel Command
United States Air Force

10. SPONSORING/MONITORING AGENCY ACRONYM(S)
AFRL/RQHF

11. SPONSORING/MONITORING AGENCY REPORT NUMBER(S)
AFRL-RQ-WP-TR-2019-0183

12. DISTRIBUTION/AVAILABILITY STATEMENT
DISTRIBUTION STATEMENT A. Approved for public release. Distribution is unlimited.

13. SUPPLEMENTARY NOTES
PA Clearance Number: 88ABW-2019-5258; Clearance Date: 14 Nov 2019.

14. ABSTRACT
This final technical report summarizes activity on AFRL 6.1 laboratory task LRIR 15RQCOR102 for the last fiscal year of this activity, 2019. During this year, the transition zone length on the HIFiRE-5b flight was assessed and high-fidelity simulation of transition induced by discrete roughness in the presence of noise was executed. Results for HIFiRE-5b showed that the transition zone length was relatively short, generally less than the fully laminar length preceding transition. Transitional heating overshoot was observed on some parts of the vehicle. High-fidelity simulations of the HIFiRE cone were able to reproduce transition trends due to roughness and wind tunnel noise that were observed in ground test.

15. SUBJECT TERMS
boundary layer transition, hypersonic, flight test, simulation

16. SECURITY CLASSIFICATION OF: a. REPORT	b. ABSTRACT	c. THIS PAGE	17. LIMITATION OF ABSTRACT:	18. NUMBER OF PAGES	19a. NAME OF RESPONSIBLE PERSON (Monitor)
Unclassified	Unclassified	Unclassified	SAR	63	Roger L. Kimmel
					19b. TELEPHONE NUMBER (Include Area Code) (937) 255-8295

Table of Contents

List of Figures

List of Tables

Acknowledgments

This work was supported by the Air Force Office of Scientific Research under Laboratory Research Initiation Request 15RQCOR102, managed by Ivett Leyva.

1. Overview

This final technical report summarizes activity on AFRL 6.1 laboratory task LRIR 15RQCOR102 for the last fiscal year of this activity, 2019. References [1 - 4] summarize prior-year activity on this task. During fiscal year 2019, the task produced two primary bodies of work. First, analysis of the HIFiRE-5b flight tests documented the transition zone length, transitional heating overshoot and produced estimates of turbulent spot generation rate [5]. Second, high-fidelity computations of the HIFiRE-1 model demonstrated the potential for using simplified noise models to replicate transition trends [6].

This analysis of HIFiRE-5b flight data revealed a relatively short transition zone length (the distance between transition onset and fully turbulent flow), generally less than the laminar length preceding transition. Also, transitional heating overshoot appeared on the vehicle at some locations, verifying that this phenomenon occurs in flight and is not an artifact of the wind tunnel environment. Section 2, which describes this work, is reproduced largely from reference [5].

In preparation for high-fidelity simulation of the HIFiRE-5b transition process, high-fidelity computations simulated experiments performed at the Purdue University Mach 6 quiet wind tunnel on the HIFiRE-1 cone. This effort examined the HIFiRE cone at 0° and 6° angle of attack, with and without intentionally added acoustic noise. The model geometries contained smooth surfaces and discrete trip elements emulating the configurations tested in the wind tunnel. Broadband acoustic noise was introduced in the computations between the shock and the model surface in an attempt to emulate wind tunnel disturbance environment that had been processed through the model bow shock. Results indicated that the computations were capable of reproducing the wind tunnel transition trends with disturbances and roughness. This procedure perhaps holds the potential to, with some calibration, reproduce wind tunnel and flight noise effects without having to compute the interaction between free stream disturbances and the vehicle bow shock. Section 3, which describes this work, is largely reproduced from reference [6].

In addition to the projects described above, additional, unpublished work occurred during fiscal year 2019. Experiments demonstrated the ability for high-speed imaging in the AFRL Mach 6 Ludwieg tube. High-fidelity computations of the HIFiRE-5 configuration, including noise fields, were executed. Additional high-fidelity computation of the BOLT configuration revealed the impact of joint steps on the mean BOLT flowfield. These efforts will be documented in future works as they become more mature.

2. HIFiRE-5b Transitional Zone Length, Transitional Heating Overshoot and Turbulent Spot Generation Rate.

2.1. Background

The effect of wind tunnel noise on boundary layer transition location is well-known. The impact of the wind tunnel environment on other aspects of hypersonic transition is less understood. In particular, the impact of wind tunnel noise on the length of the transition zone and transitional heating overshoot is not well-defined. The transitional zone is defined as the region between onset of transition and end of transition. Conventional wind tunnel data indicate a rather extended transition zone region, often equal to the length of the laminar zone preceding it. Quiet supersonic wind tunnel data, however, can show a very short transitional zone length, as little as 10% of the laminar length preceding it [7]. The length of the transitional zone impacts vehicle design in several ways. An extended transitional zone, as observed in wind tunnels, could place a large region of the vehicle in transitional flow. A very short transition length creates high spatial temperature gradients, and might contribute to thermal stress on a vehicle.

Another phenomenon observed during transition is overshoot. Overshoot is the tendency of parameters such as heating, skin friction, pressure fluctuations, and so on, to rise above their expected equilibrium turbulent values near the end of the transition process, then relax to their expected turbulent values. Since overshoot heating by definition exceeds turbulent downstream heating, it represents a stressing design case, and is therefore worthy of study. The physics behind overshoot are poorly understood, and the impact of wind tunnel noise on overshoot is even murkier.

Given the importance of transitional zone length and overshoot, and the paucity of flight data regarding them, it was logical to see if the HIFiRE-5b could reveal how these phenomena behaved in flight. In addition, turbulent spot generation rates could be inferred from the transition zone length. This section describes transitional zone length, heating overshoot and turbulent spot generation rate estimates for HIFiRE-5b during hypersonic flight.

2.2. Flight-Test Trajectory and Attitude

HIFiRE-5b launched in May 2016 from the Woomera Test Range in Australia. Reference [8] describes the flight in detail. Both rocket stages operated as expected and the as-flown trajectory was nominal. The as-flown freestream Mach number, velocity, unit Reynolds number, and altitude during the terminal descent are shown in Figure 1. The period of time from 513 to 518 s after launch yielded the most interesting boundary-layer transition results. During this time period, the Mach number was relatively steady, within the interval of 7.7 to 7.9. The freestream unit Reynolds number increased monotonically from 5 to 27 × 10^6/m as the flight vehicle descended into denser regions of the atmosphere.

The vehicle was spun at a low rate to reduce trajectory dispersion. Cant angle on the first and second-stage fins caused the vehicle to spin passively. Because of this, the payload was rolling throughout the entire trajectory. Vehicle attitude was first derived using the on-board (GPS) and (IMU), as described in Ref. [9]. The GPS and IMU both suffered anomalies during the flight [8]. Fortunately, angle of attack and yaw were able to be calculated from correlations of the pressure transducer data with CFD analysis of the surface pressure distribution for various combinations of angle of attack and yaw [10, 11]. The pressure/CFD-derived vehicle attitude is preferred over the GPS/IMU method and is the source for all attitudes presented herein.

Angle of attack α and yaw β during HIFiRE-5b's descent are shown in Figure 2. Several important observations can be made from these traces. The mean angle of attack and yaw are both essentially zero. The amplitudes of the oscillations are nearly equal to one another, beginning at about 1.5° at t = 512 s ($Re = 4 \times 10^6$ /m) and decreasing to about 0.5° at t = 519 s ($Re = 37 \times 10^6$ /m). As shown in Ref. [12], even these small non-zero angles introduce noteworthy asymmetry in HIFiRE-5's surface heating distribution, by virtue of an altered boundary-layer transition front. The oscillation frequency increases slightly, from about 6 Hz to 7 Hz. The rate of precession is very small compared to the forward velocity, so the swirling component of the freestream velocity is regarded as zero. Angle of attack and yaw are about 90° out of phase for the entirety of the descent. For this reason, there is no instant at which both α and $\beta \approx 0$ until $t > 519$ s, by which time the boundary-layer is fully turbulent over the instrumented portion of the vehicle.

In Ref. [13], heat-flux traces were plotted as a straightforward function of time. Naturally, the oscillating attitude caused oscillating heat flux for all sensors. The magnitude and nature of these heat-flux oscillations varied depending on the sensor azimuth. To discriminate between the effects of time-varying attitude and heat flux, a method was developed to selectively sample the data to fix either zero angle of attack or yaw, as described in Refs. [14, 15]. Figure 3 shows the yaw angle at zero angle of attack and Figure 4 shows the angle of attack at zero yaw. The times at which α and β are positive or negative are grouped as distinct subsets. The net result of dividing the data set this way is that instead of plotting heat flux for $\approx$1.5° variations of angle of attack and yaw, heat flux can be plotted for zero angle of attack and slightly varying yaw ($\approx$0.3° peak-to-peak variation), or zero yaw and slightly varying angle of attack. The downside of the sub-sampling is that the thermocouples, which were originally sampled at 400 Hz, now only yield approximately 25 data points per second, or about six points per second for each of the four data sets ($\alpha = 0, \beta > 0$; $\alpha = 0, \beta < 0$; $\alpha > 0, \beta = 0$; $\alpha < 0, \beta = 0$). There is no time at which angle of attack and yaw are simultaneously zero.

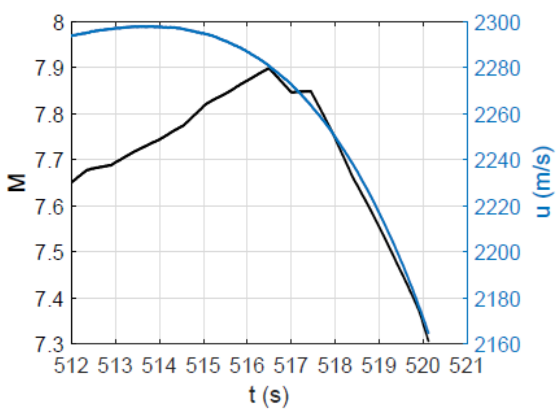

(a) Freestream Mach number and velocity.

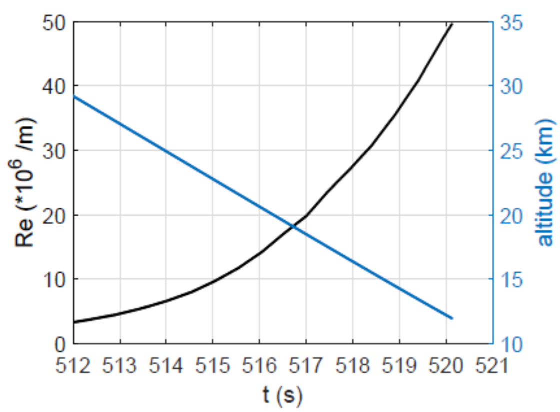

(b) Freestream unit Reynolds number and altitude.

Figure 1 As-flown trajectory.

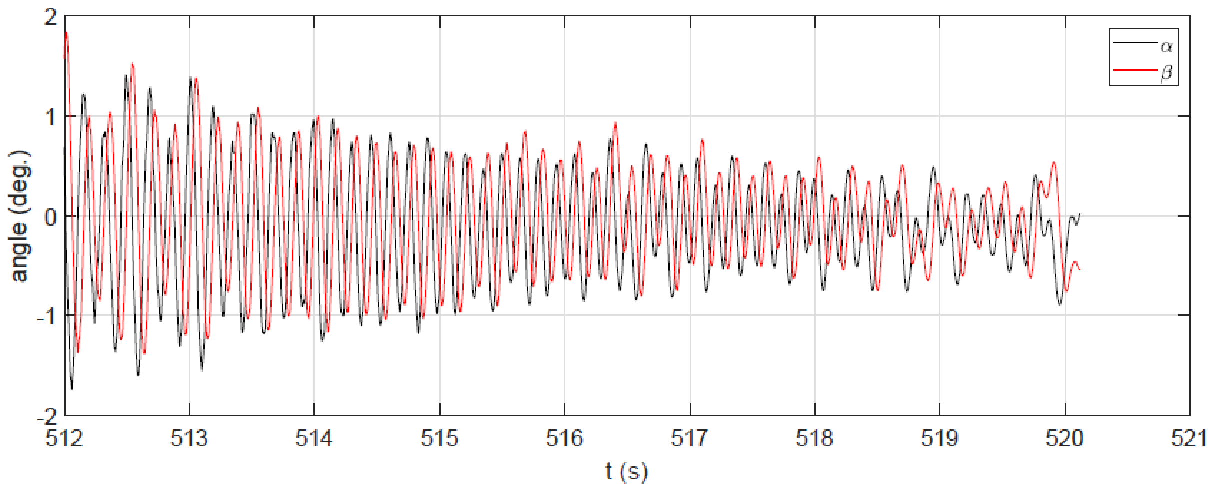

Figure 2 HIFiRE-5b attitude.

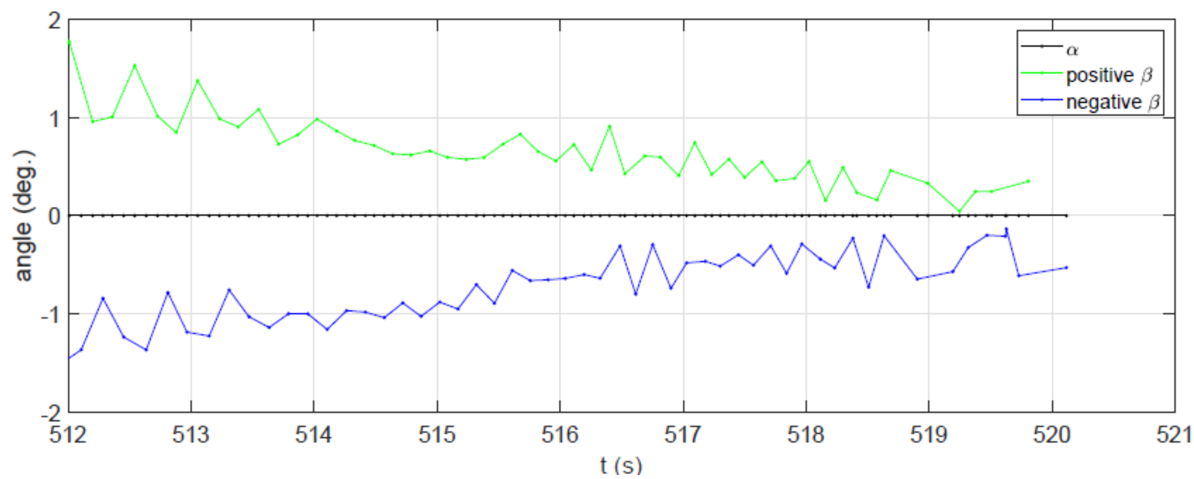

Figure 3 Yaw angle at zero angle of attack.

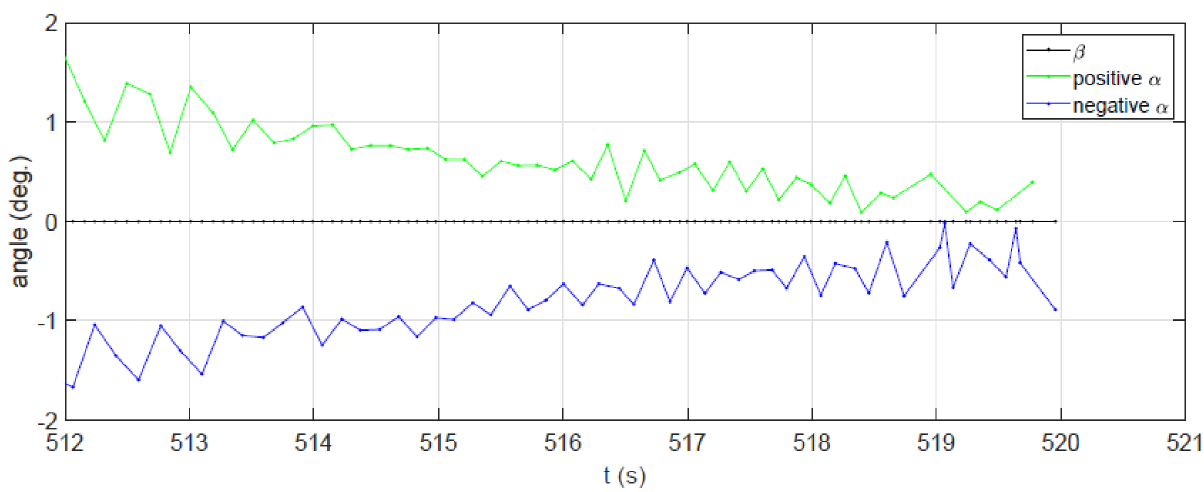

Figure 4 Angle of attack at zero yaw.

2.3. Data Reduction Methodology

2.3.1. Calculation of Heat Flux from Thermocouple Data

A 10 ms moving average was applied to the thermocouple outputs to reduce noise before calculating the heat flux. The moving average acts effectively as a low-pass filter with a 3-dB reduction at 80 Hz. The average was calculated over points forward and backward in time, to avoid phase-shifting the output. Laboratory bench experiments with Medtherm thermocouples mounted identically to the HIFiRE-5b installation demonstrated that these transducers were capable of easily resolving temperature fluctuations resulting from a 10 Hz square-wave heating input at heating rates comparable to laminar reentry levels[16]. The thermocouples on HIFiRE-5b therefore possessed adequate bandwidth to resolve heating fluctuations arising from the vehicle spin, which was approximately 5 Hz. Performing the inverse analysis largely accounts for any phase shift created by the thermocouple response.

Figure 5 shows representative temperature histories for the pair of thermocouples at x = 600 mm, ϕ = 90°. The 0.01-s moving-average filter has already been applied to these traces. The large surface-temperature increases during ascent and descent are readily apparent; the rate of temperature change at high altitude is much lower, as expected. All back-face thermocouples were shifted at t = 400 s to equal the front-face temperature at that location, thereby ensuring that the heat flux is identically zero shortly before reentry. The shift was in all cases less than 11.5 K; in the Figure 5 case, it was 1.4 K. The shift was employed because the thermocouple signals tended to drift during launch, ascent, and the 5-minute-long exoatmospheric portion of the trajectory. Without it, some thermocouples would have indicated negative heat flux during descent. The correction was especially critical for the low heating rates encountered at low freestream Reynolds numbers (high altitudes). The front-face thermocouple output voltage saturated at t = 518.5 s, leading to a false indication of decreasing heat flux for the brief remainder of the flight. The distinct change in the slope of the temperature history in Figure 5b indicates transition at t = 514.6 s, even without the reduction of temperature to heat flux.

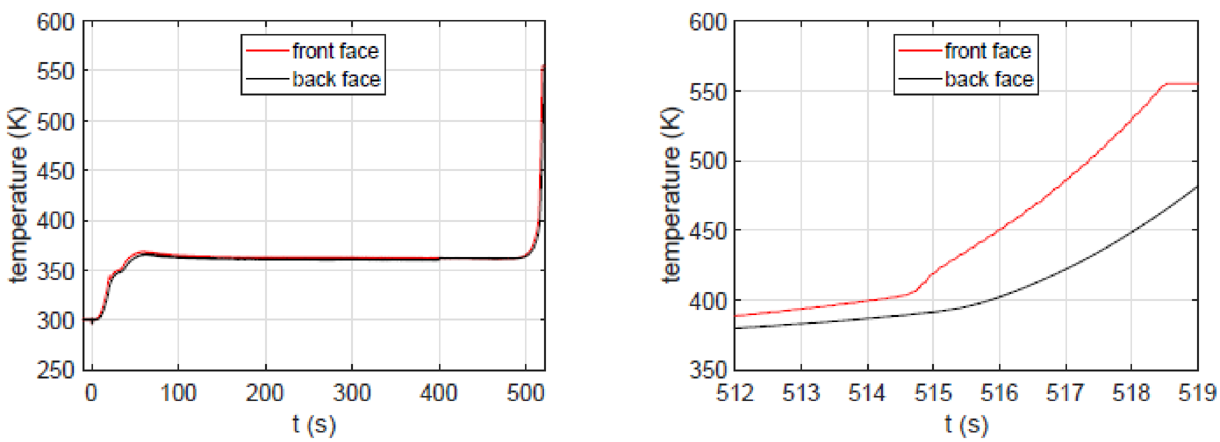

(a) Entire flight.

(b) Descent only.

Figure 5 Front- and back-face thermocouple temperature measurements. x = 600 mm, ϕ = 90°.

Heat flux was calculated from the front- and back-face thermocouple temperatures by solving the transient 1-D heat equation. The FORTRAN QCALC subroutine written by Boyd and Howell [17] was translated to Matlab for this purpose. QCALC assumes one-dimensional heat transfer and uses a second-order Euler explicit finite difference approximation to solve for the temperature distribution through the vehicle shell; heat flux is obtained from a second-order approximation to the derivative of the temperature profile at the outer surface. The code provides the options of solving in Cartesian, cylindrical, or spherical coordinates, and applying a constant or time-varying back-face temperature or the adiabatic boundary condition. For the HIFiRE-5 data reduction, the equation in cylindrical coordinates was used with the local radius of curvature, wall thickness, and material properties. The front- and back-face thermocouples provided the boundary conditions.

Figure 6 shows the heat flux calculated from the thermocouple data shown in Figure 5 The nonzero heat flux during high-altitude flight can be at least partially attributed to axial heat conduction through the model shell, belying the assumption of strictly one-dimensional heat flux. Several thermocouple voltages drifted during flight, which is another contributor.

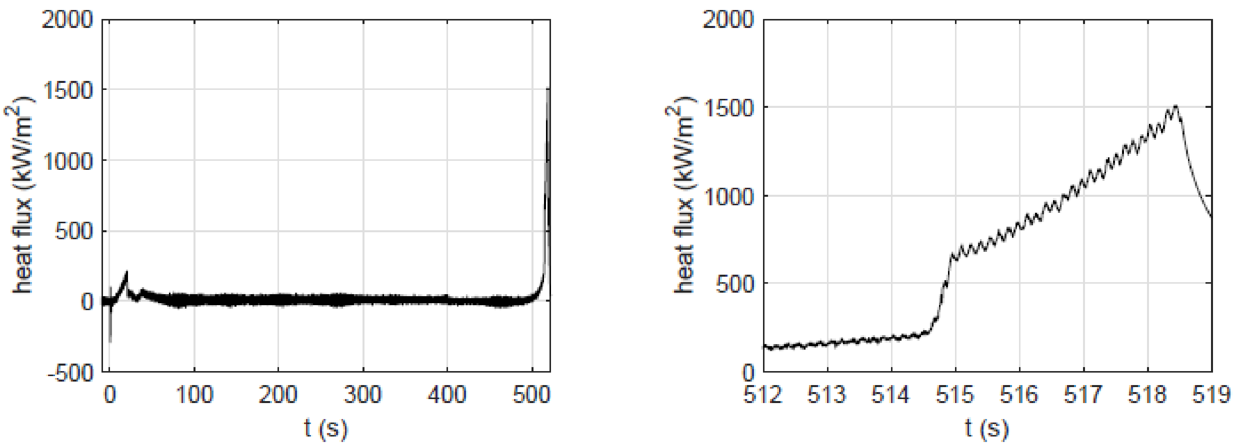

(a) Entire flight. **(b) Descent only.**

Figure 6 Heat flux calculated from thermocouple data. x = 600 mm, ϕ = 90°.

The primary error sources for heat transfer, as derived from the thermocouple data, were thermocouple drift and lateral conduction. The sensitivity of the derived heat transfer to these error sources was estimated using the methodology described in Ref. [11]. This analysis showed that, between 510 and 520 s, the primary error source was lateral conduction, which contributed less than 11% error for fully laminar flow and 8% for turbulent flow. The response to lateral conduction during transition was more complex. Because thermocouples were shifted to force zero heat transfer at the beginning of reentry, the error due to drift was estimated to be less than 1 K. Analysis using the Ref. [11] methods indicated that a 1-K shift in temperature led to an error of less than 9% for laminar heating and 2% for turbulent heating. Overall, heating uncertainty is therefore estimated to be approximately 20% for laminar heating and 10% for turbulent. The entire heat-flux calculation procedure was carried out for the full thermocouple temperature histories. The sub-sampling was only executed on the reduced heat-flux data. Filtering over 0.01 s means that data for 0.2° variation of angle of attack and yaw is averaged together.

2.3.2. Non-dimensionalization, Filtering, and Transition Assessment

The majority of results herein are presented as a non-dimensional Stanton number instead of dimensional heat flux. Stanton number *St* is defined using freestream stagnation temperature, rather than a recovery temperature, for convenience:

$$St = \frac{\dot{q}''}{\rho_\infty u_\infty c_p (T_0 - T_{wall})} \quad (1)$$

The recovery factor is about 0.83 for a laminar flat plate at Mach 7.7[18]. Defining Stanton number based on (T_0 - T_{wall}) thus yields a value approximately 20% greater than that based on the difference between adiabatic wall and boundary layer edge temperatures. The conventional definition of *St* also requires the (spatially varying) edge conditions. Rather than relying on computations of these values and an estimate for the recovery factor, past work reporting HIFiRE flight tests have used this alternative definition based on measured quantities.

In Ref. [13], boundary-layer transition was determined by manual inspection of the heat-flux time traces. The dependence of heat flux on vehicle angle of attack and yaw, plus the noise in the signal, limited the accuracy with which an algorithm could automatically identify transition. As will be seen below, controlling for vehicle attitude significantly reduces the oscillatory heat-flux amplitudes. These steadier time traces were more amenable to filtering without loss of high-frequency content. This filtering was calculated with Matlab's built-in smooth function with the 'loess' method: "local regression using weighted linear least squares and a 2nd degree polynomial model". It was determined heuristically that a smoothing span of 10% of the data record — about 0.7 s, or a *Re* variation of 3×10^6 to 5×10^6/m — retained the local extrema while reducing noise.

The times of transition onset and end were determined from these filtered Stanton-number traces. The time of minimum *St* is inferred to be the time of transition onset and the time of maximum *St* is inferred to be the time of transition end. The preliminary assessment was automated, but then all *St(Re)* profiles were manually inspected to verify the reasonableness of the algorithm. Twenty-three of the 440 (5.2%) automated transition assessments were found to be corrupted by noisy *St* profiles — for example, by a burst of noise in the thermocouple signal, or very low signal levels at low *Re*. A manual determination was substituted for the automated one in these cases.

2.4. Results

2.4.1. Symmetry Check and Effect of Yaw on Heat flux

Early analysis of HIFiRE-5b data provided evidence that sensors mirrored across a plane of symmetry (e.g., at ϕ = 90 and 270°) yielded heat-flux traces that were 180° out of phase with one another. This behavior was a motivation for extracting the attitude-controlled subset of data. Now that they have been created, this observation has been revisited. In Figure 7, the heat flux histories are plotted for the thermocouples at x = 400 mm, ϕ = 90 and 270°. Figure 10a shows the full descent past saturation of the thermocouples; figure 10b focuses on the period from just before transition onset to after transition end. The black and green lines show the experimental heat flux for these two thermocouple pairs; the blue and red lines indicate laminar and turbulent empirical predictions derived from wind tunnel data for a sharp elliptic cone. In Figure 7b, circles mark the times at which the angle of attack was zero and yaw was positive (i.e., ϕ = 90° to windward, 270° leeward) and marks negative yaw. Indeed, peak heating on one leading edge correlates well with minimum heating on the opposite. However, the mean heat flux differs by about 8% between the two sensors in the laminar, transitional, and turbulent regimes. This difference is in line with the expected uncertainty for these sensors and data reduction technique (see Section 2.3.1).

This symmetry was observed clearly along the leading edges. Figure 8 shows the Stanton number histories at $x = 300, 400, 600$, and 800 mm. In most cases, the laminar and turbulent empirical fits do well predicting the mean variation of the observed heating rates, although the empirical laminar heating rates are 30% lower than measured. The same out-of-phase behavior on opposite leading edges occurs for all heating traces.

It was argued in Refs. [14, 15] that this out-of-phase behavior primarily arose from the oscillating vehicle attitude. Because the empirical fit captures the time (and thus Reynolds number) variation of the heating rates, they were used to detrend the fluctuating heating rates, leaving only the higher frequency oscillations (i.e., the 'AC-coupled' component of the signal). This makes it possible to better quantify and assess this explanation for the time-varying heat flux. The data were divided into laminar (before transition onset) and turbulent (after transition end) portions (see Refs. [13]), and the pertinent empirical fit was used for each. Figure 9 is representative of the result of the detrending. It shows the detrended Stanton number ($St_{flight} - St_{fit}$) and yaw angle β as a function of time for the sensors on the leading edges at x = 600 mm. In Figures 13 and 14, the time dependence has been eliminated — they show the detrended St as a function of yaw angle β at x = 300 and 600 mm, respectively. A linear interpolation of $\beta(t)$ was used to obtain β at the specific time of each St data point. Each point represents one sample of detrended flight-test data. The solid lines in Figure 10 and Figure 11 are the best-fit lines.

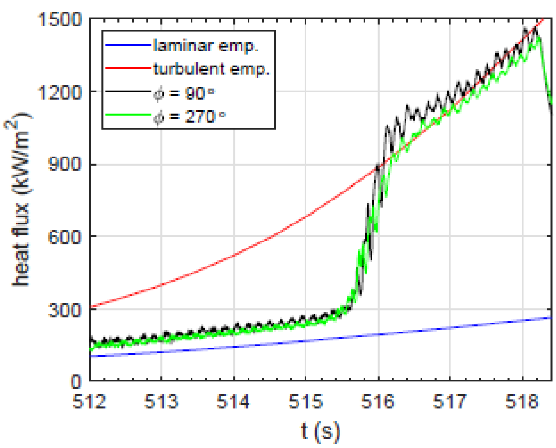

(a) Full descent.

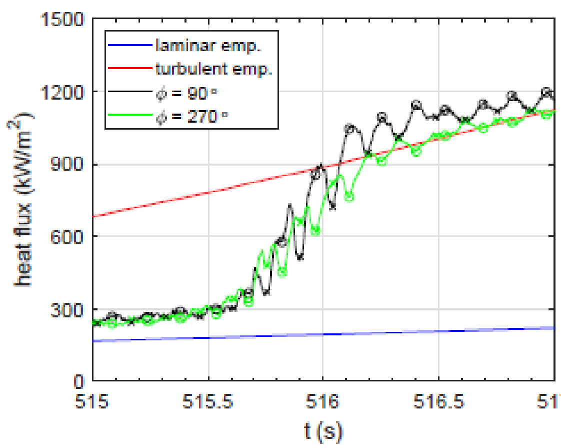

(b) During transition.

Figure 7 Comparison of leading edge heat flux history. x = 400 mm.

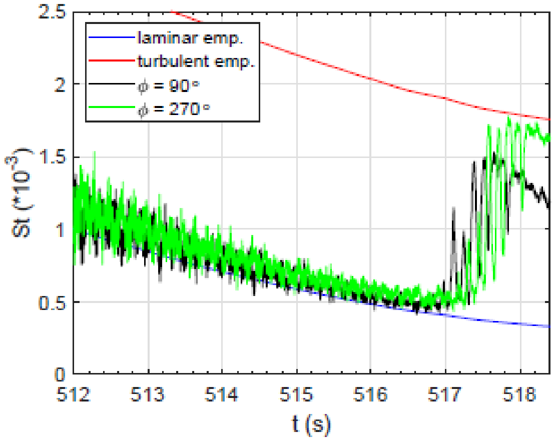

(a) x = 300 mm.

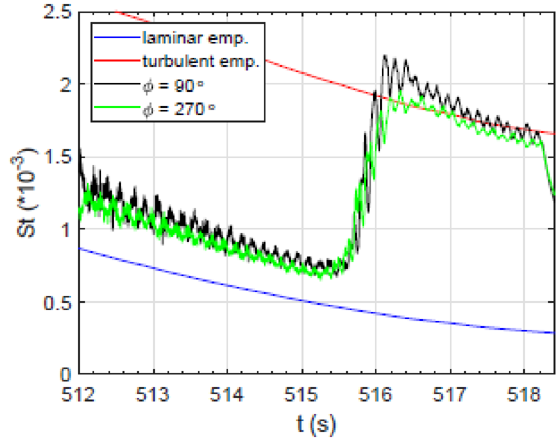

(b) x = 400 mm.

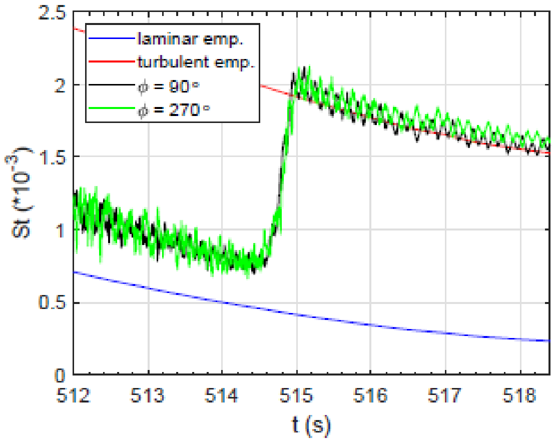

(c) x = 600 mm.

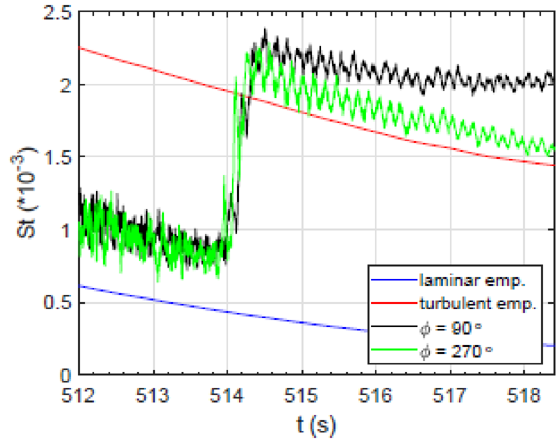

(d) x = 800 mm.

Figure 8 Non-dimensional heat flux along leading edges.

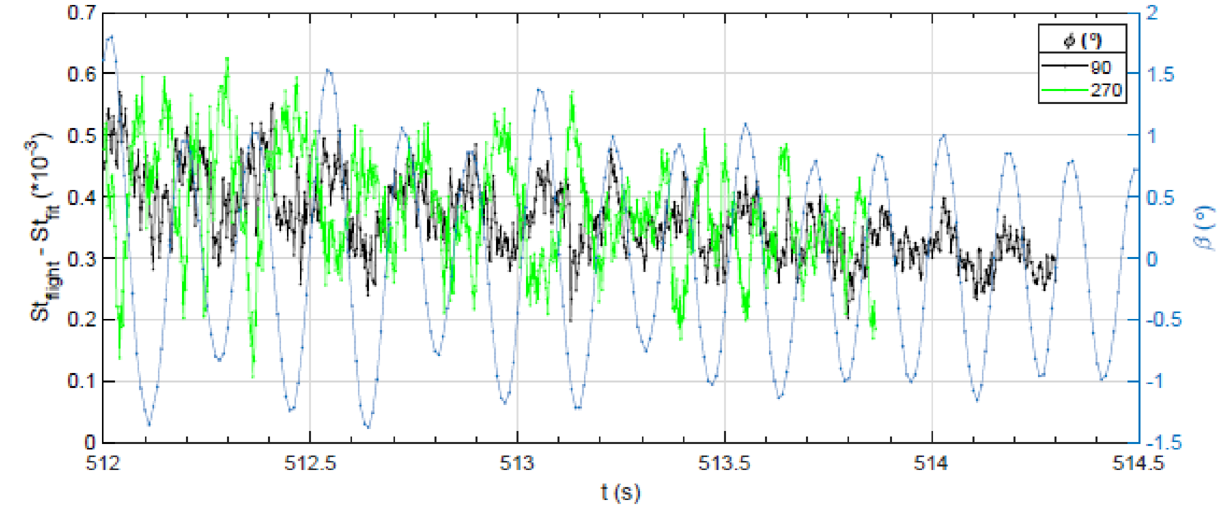

(a) Laminar portion.

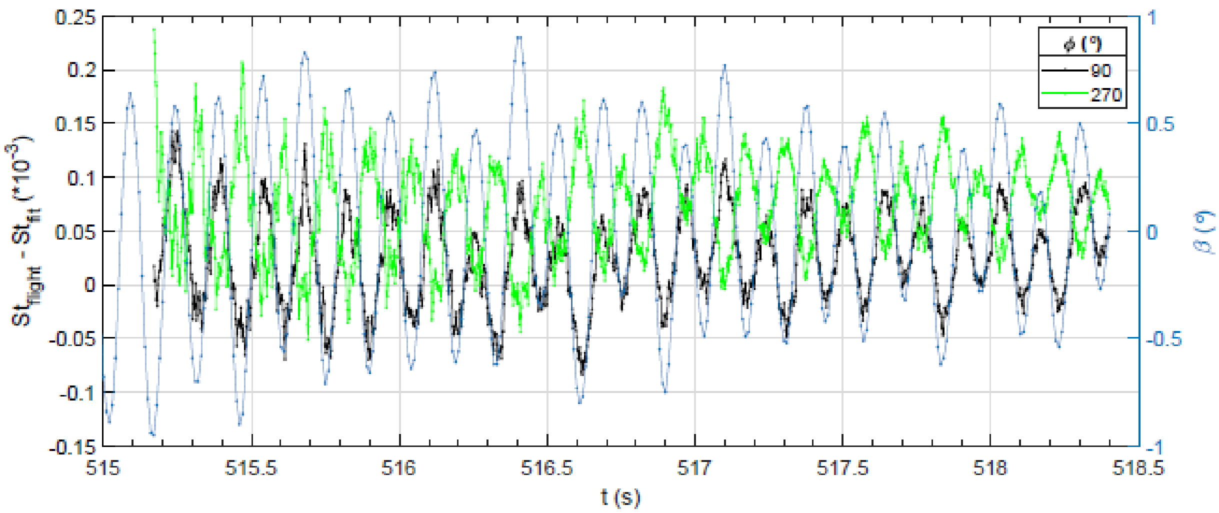

(b) Turbulent portion.

Figure 9 Detrended non-dimensional heat flux. *x* = 600 mm.

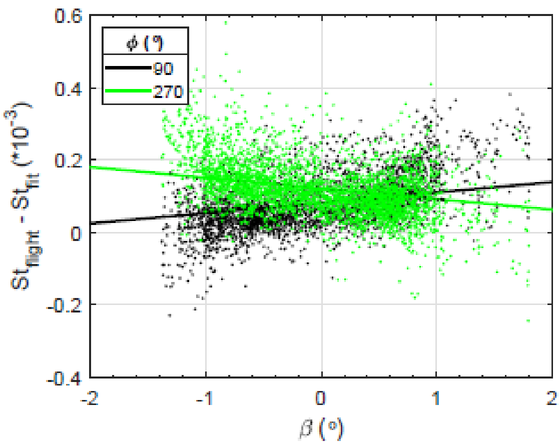

(a) Laminar portion.

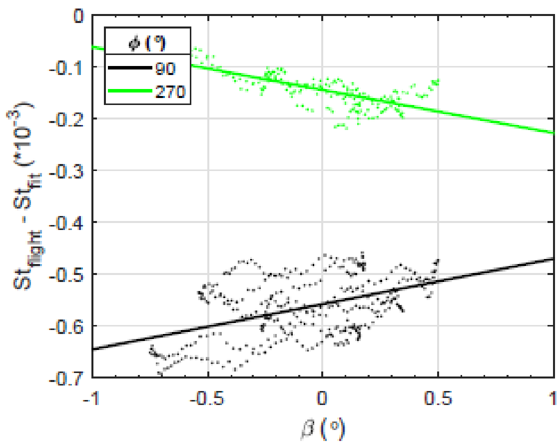

(b) Turbulent portion.

Figure 10 Effect of yaw angle on heat flux. $x = 300$ mm.

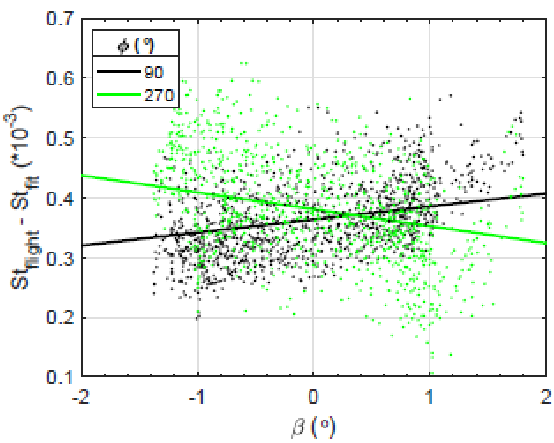

(a) Laminar portion.

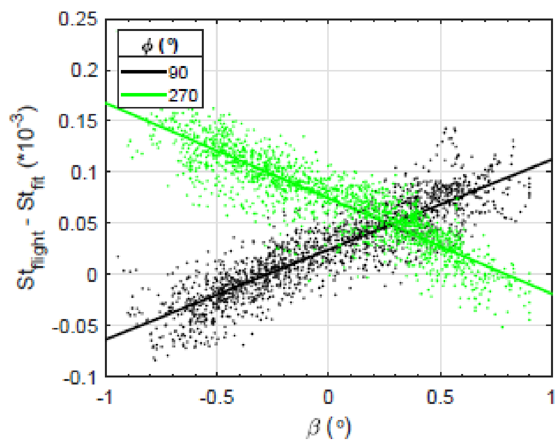

(b) Turbulent portion.

Figure 11 Effect of yaw angle on heat flux. $x = 600$ mm.

The results of the linear regression, including its slope, intercept, and correlation coefficient R, are summarized in Table 1. They are consistent with the hypothesis that the oscillations in the heating rate are due to oscillating vehicle attitude. The best-fit lines for sensors at the same axial station, but 180° apart azimuthally, have slopes of opposite sign and approximately equal magnitude (differences of 25% or less). The slopes indicate the sensitivity of heat flux to small yaw angles as measured in flight, a potentially useful quantity to know when designing a vehicle's thermal protection or flight control systems. The intercepts are one-number assessments of how well the empirical fits match the flight data. Ideally, they would all be zero, which would indicate that the empirical correlation matches the slowly varying ('DC-coupled') in-flight heating. However, the fit predicting laminar heating along the leading edges is systematically low (an observation also reported in Ref. [13]).

In every case, heating along the $\phi = 90°$ ray correlates with yaw angle, whereas heating along the $\phi = 270°$ ray is anti-correlated. In most cases, R^2 for the two rays match within 20%; the only exception is the turbulent correlation at $x = 300$ mm. The explanation for this difference is visible in Figure 8a: the slope of the heating detected in flight does not match the empirical correlation as well as for other sensors. This results in greater dispersion of the data, as seen in Figure 10b. The cause of the lower than expected heating indicated by this thermocouple pair is unclear, but thermocouple drift is the most likely cause. The fit agrees well with the sensor at ϕ = 270°, so it is not suspected to be seriously in error. The mean laminar heating rates for these sensors are nearly equal, suggesting that the thermocouple drift occurred during the transitional phase (t = 517.0–517.6 s), when the temperatures rose significantly.

Table 1 Correlation of heating fluctuations with yaw angle.

x (mm)	state	azimuth (°)	slope ($\cdot 10^{-3}$ /°)	intercept ($\cdot 10^{-3}$)	R	R^2
300	laminar	90	0.057	0.082	0.54	0.29
300	laminar	270	−0.059	0.12	−0.51	0.26
300	turbulent	90	0.050	−0.53	0.38	0.15
300	turbulent	270	−0.038	−0.13	−0.51	0.26
600	laminar	90	0.044	0.36	0.55	0.30
600	laminar	270	−0.057	0.38	−0.50	0.25
600	turbulent	90	0.088	0.024	0.88	0.78
600	turbulent	270	−0.093	0.074	−0.90	0.80

Among the limited subset of sensors analyzed, the correlation between detrended St and β is highest for the turbulent heating rate at x = 600 mm. The ϕ = 90° and 270° sensors show almost equal and high R^2 values (0.78 and 0.80, respectively). The high correlation is apparently due to the high signal-to-noise ratio for this pair of sensors combined with the effectiveness of the empirical fit to predict the dependence of St on Re. For the minimal time averaging of the temperature data, all the sensors exhibit fluctuations of a higher frequency than the attitude oscillation. This noise is typically on the order of 0.02 to 0.1×10^{-3} in St. The relatively large sensitivity of St to β (0.1×10^{-3} per degree) produces the best correlated result.

2.4.2. Impact of Filtering on Heat-Flux Measurements

As described in section 2.3.1, a 10 ms moving average was applied to the thermocouple outputs to reduce noise before calculating the heat flux. This filter has been applied consistently for all analyses of HIFiRE-5b heat flux [13, 14, 15]. Unfiltered and filtered Stanton-number histories are plotted side-by-side in Figure 12. Three filter durations are shown: the baseline 10 ms, a longer 20 ms, and an extra-long 50 ms. The filters' effects are apparent and unsurprising: there is a clear reduction in the noise, but the extrema in the signal are lost.

The preceding analysis of heat flux as a function of yaw angle provides an opportunity to investigate the impact of the filtering and assess whether it affects the conclusions drawn from the data. It is expected that the unfiltered residual Stanton number would have a lower correlation with yaw because of the poorer signal-to-noise ratio, but that the sensitivity of residual Stanton number to yaw would be higher, because the signal's extrema will not be lost to the averaging. Figure 13 contains plots of the residual turbulent Stanton number as a function of yaw for unfiltered thermocouple data and data with 10, 20, and 50 ms moving-average filters. The results of the linear regression are shown in Table 2.

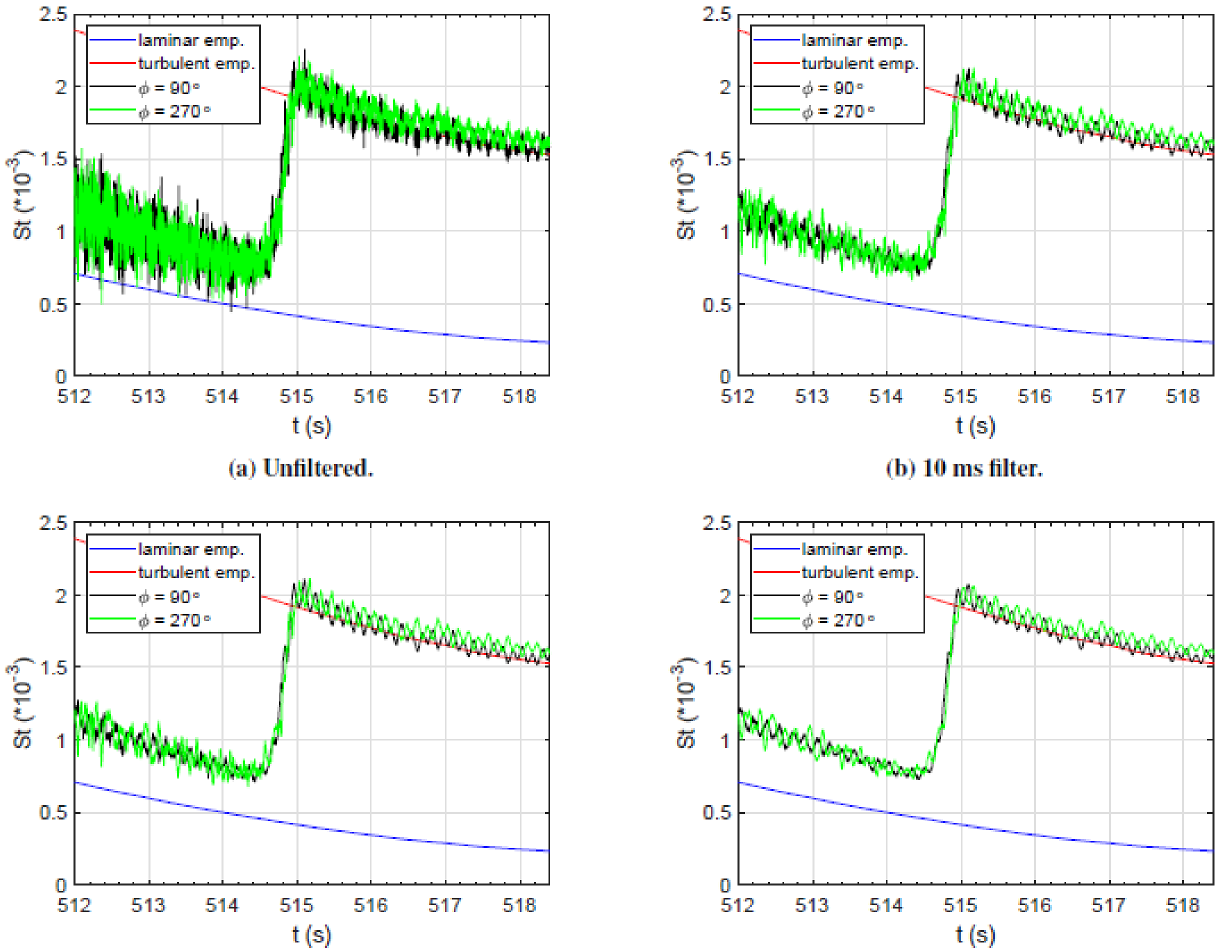

(a) Unfiltered.

(b) 10 ms filter.

(c) 20 ms filter.

(d) 50 ms filter.

Figure 12 Non-dimensional heat flux along leading edges. *x* = 600 mm.

The anticipated effects of the filter duration are borne out by the data. Compared to unfiltered data, the baseline 10 ms filter has less sensitivity, but the reduction is only 2%. R^2, however, increases substantially for this filtering, from 0.45 to 0.78. Doubling the filter length to 20 ms loses an additional 2% of sensitivity and increases R^2 slightly, to 0.81. With the 50 ms filter, *St(t)* exhibits very little noise (Figure 12d). The correlation between residual Stanton number and yaw angle is essentially unchanged from the 10 ms filter, because the data's scatter is due to longer-period deviations from the empirical fit. The indicated sensitivity of heating to yaw angle is negatively affected by this long filter duration; it is 17% lower with the 50 ms filter than with the 10 ms filter. Among the various filter options examined, the baseline 10 ms duration offers the best balance of noise rejection and sensitivity.

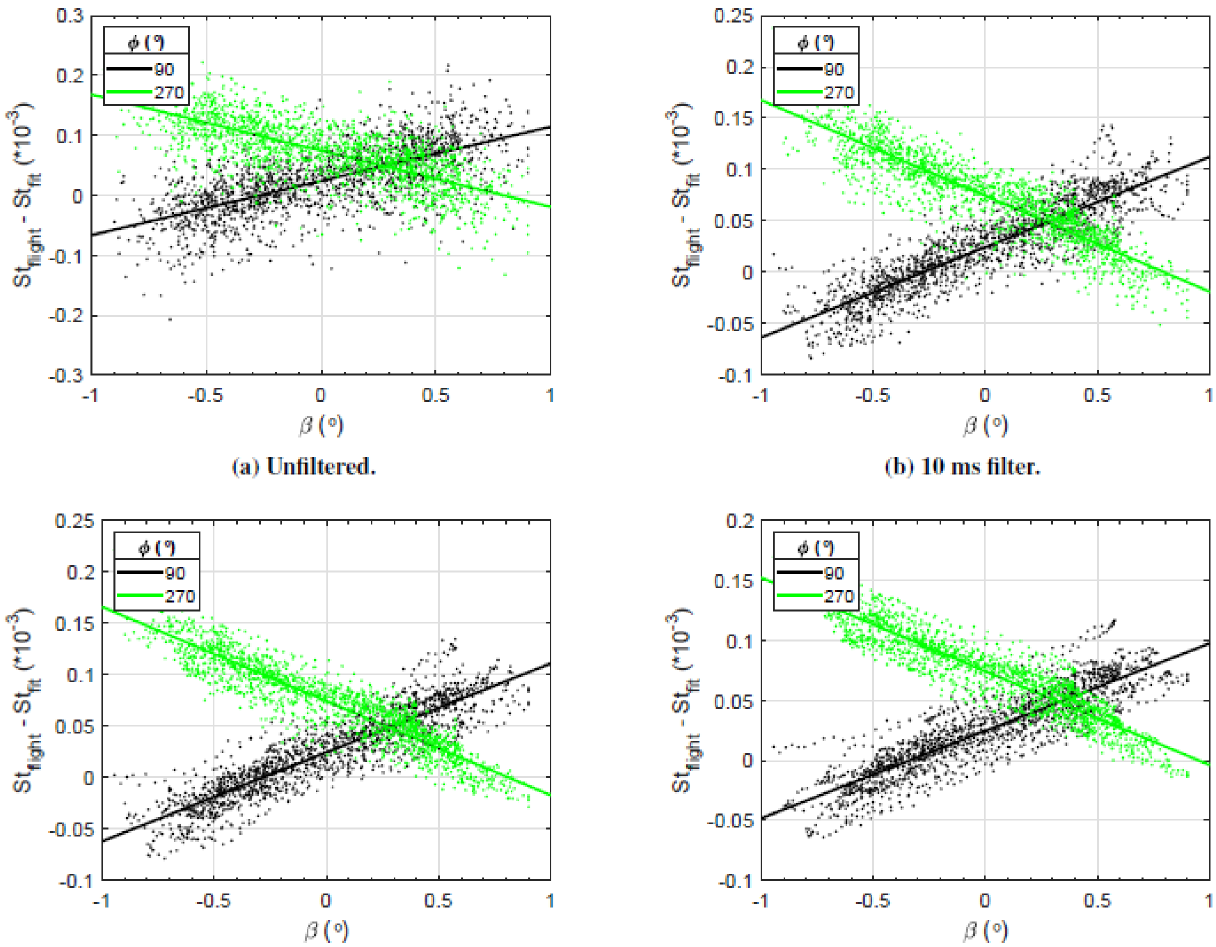

(a) Unfiltered.
(b) 10 ms filter.
(c) 20 ms filter.
(d) 50 ms filter.

Figure 13 Effect of yaw angle on heat flux. x = 600 mm.

Table 2 Correlation of heating fluctuations with yaw angle for various filter durations.

x (mm)	state	azimuth (°)	filter (ms)	slope ($\cdot 10^{-3}$ /°)	intercept ($\cdot 10^{-3}$)	R	R^2
600	turbulent	90	0	0.090	0.024	0.67	0.45
600	turbulent	90	10	0.088	0.024	0.88	0.78
600	turbulent	90	20	0.086	0.024	0.90	0.81
600	turbulent	90	50	0.073	0.025	0.88	0.78

2.4.3. Streamwise Heat-Flux Profiles

Most sets of data for hypersonic flows contain coarsely spaced flow conditions and fine spatial resolution. For example, a computational simulation for a given flow condition yields data at the grid spacing; the number of flow conditions tested is very small compared to the number of grid points. For ground-test experiments with an optical technique such as infrared thermography or temperature-sensitive paint, the situation is similar. Perhaps a camera's spatial resolution isn't as fine as a CFD grid's, perhaps time allows collecting data at more flow conditions, but there are still many more data points at one test condition than there are conditions in the test matrix. For a set of flight data, however, the situation is exactly reversed: data are collected at many flow conditions, but at relatively few spatial locations. For example, HIFiRE-5b had a very large number of sensors for a flight-test vehicle: 137 thermocouple pairs, plus single thermocouples, heat-flux gauges, pressure transducers, etc. The thermocouple pairs were sampled at 400 Hz throughout the flight; freestream unit Reynolds number increased from less than 5×10^6/m to greater than 50×10^6/m over about 8 seconds. Viewed this way, over 3000 test conditions were sampled during the descent alone.

For this reason, the primary format in which the HF5b flight-test data have been presented emphasizes the fine resolution of the flow conditions. For example, heat flux (or Stanton number) has been plotted as a function of time (or Reynolds number) for an individual sensor. Similarly, the freestream unit Reynolds number at transition can be determined with good precision for a specific position on the model; the precision with which the transition location can be determined for a given freestream unit Reynolds number is much lower. Adjustment is required for audiences accustomed to considering a pressure distribution from a CFD simulation or a heat flux profile extracted from infrared thermography. Cognizant of this difficulty, past methods of presenting the flight test data have included 'contour' plots of the surface temperature, heat flux, and boundary-layer state that were constructed by assigning the pertinent value from each thermocouple pair a pixel at its corresponding location. Thus, the areas of elevated temperature, higher heating, and the transition front can be more easily visualized. The downside to this presentation is that each figure contains data from only a single instant in time.

To facilitate comparison for varying freestream unit Reynolds numbers streamwise profiles of heat flux as a function of the axial distance from the nose tip x have been constructed. Figure 14, Figure 15, andFigure 16 contain these profiles along the $\phi = 0°$, 45°, and 90° rays, respectively. These are the three most densely instrumented rays, on which the sensors are installed in 5 cm increments. The freestream unit Reynolds number ranges from approximately 5×10^6/m to 30×10^6/m in 5×10^6/m increments. These conditions are not matched exactly; instead, the nearest time at which angle of attack or yaw is zero was selected to discriminate between the effects of varying attitude and freestream conditions. Gaps in the profiles show where data from bad sensors have been excised ($x = 0.60$ m, $\phi = 0°$; $x = 0.70$ m, $\phi = 90°$; $x = 0.80$ m, $\phi = 90°$). The laminar and turbulent heating rates are observed to steadily increase as Re increases; transition location steadily decreases.

In Figure 17, Figure 18, and Figure 19, these data have been non-dimensionalized: heat flux to Stanton number St and length to length Reynolds number Re_x. The laminar and turbulent heating rates are observed to collapse very well. Re_x at transition collapses imperfectly, which accords with the findings reported in Ref. [14] (specifically Figure 22 and its discussion). The solid and dashed black lines show the empirical correlations for laminar and turbulent boundary layers, respectively. This correlation fits St as a function of M, Re_x, and the local flow turning angle, which is a function of ϕ. The mean Mach number of the data represented in each plot was used so as to obtain laminar and turbulent St as functions of Re_x only. These straightforward correlations do a very good job predicting St and its variation with Re_x. The largest discrepancies arise from turbulent overshoot.

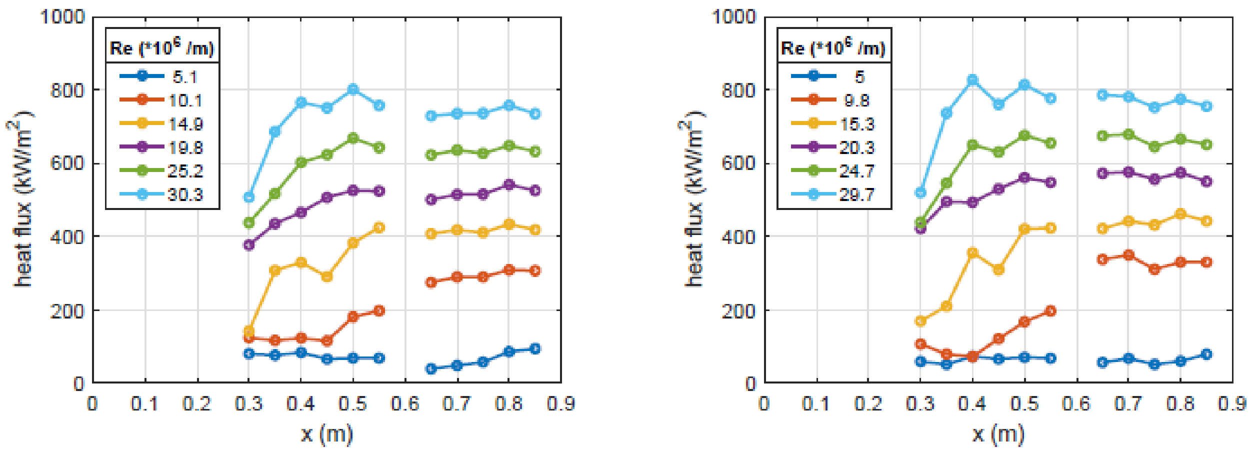

(a) $\beta = 0, \alpha < 0.$

(b) $\beta = 0, \alpha > 0.$

Figure 14 Streamwise non-dimensional heat-flux profile. $\phi = 0°$.

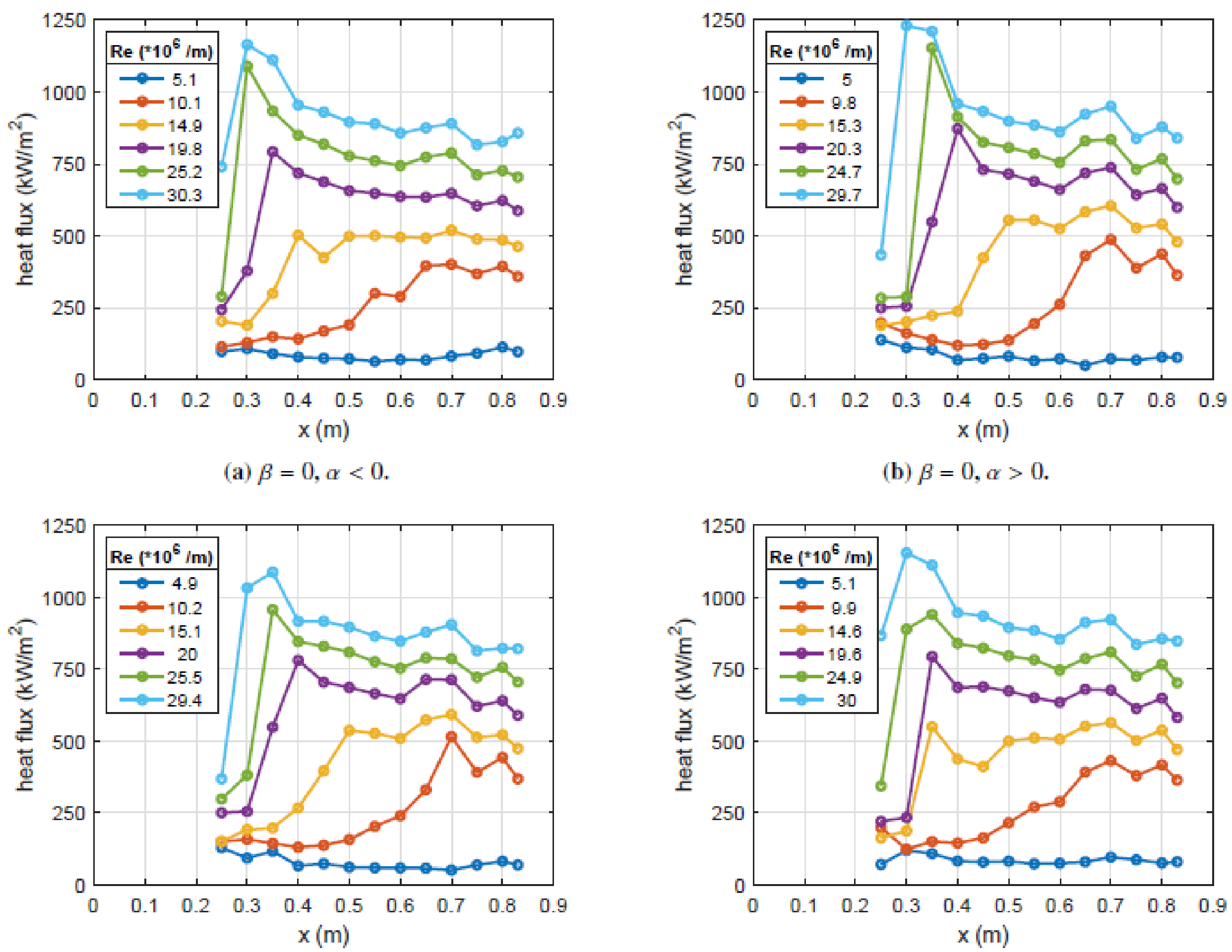

(a) $\beta = 0, \alpha < 0.$

(b) $\beta = 0, \alpha > 0.$

(c) $\alpha = 0, \beta < 0.$

(d) $\alpha = 0, \beta > 0.$

Figure 15 Streamwise non-dimensional heat-flux profile. $\phi = 45°$.

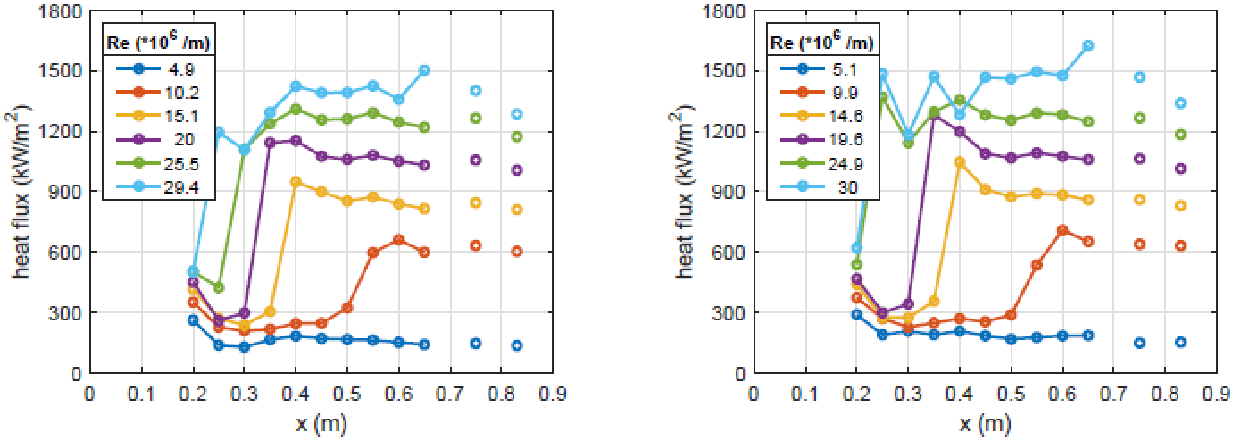

(a) $\alpha = 0, \beta < 0.$ (b) $\alpha = 0, \beta > 0.$

Figure 16 Streamwise non-dimensional heat-flux profile. $\phi = 90°$.

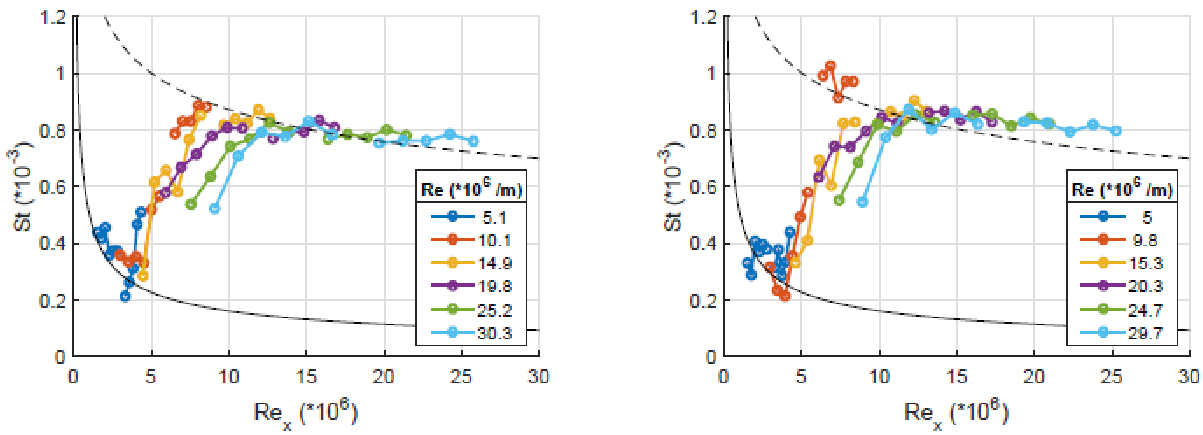

(a) $\beta = 0, \alpha < 0.$ (b) $\beta = 0, \alpha > 0.$

Figure 17 Streamwise non-dimensional heat-flux profile. $\phi = 0°$.

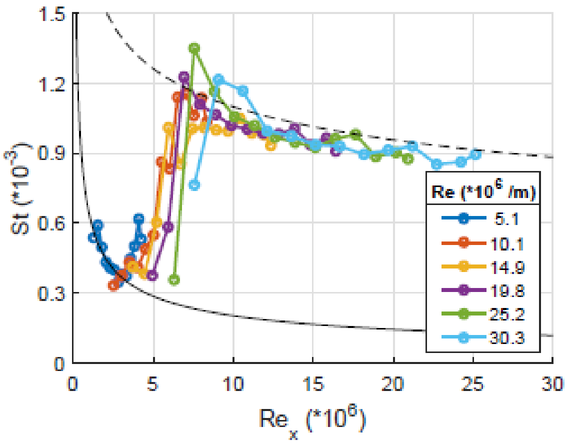

(a) $\beta = 0, \alpha < 0$.

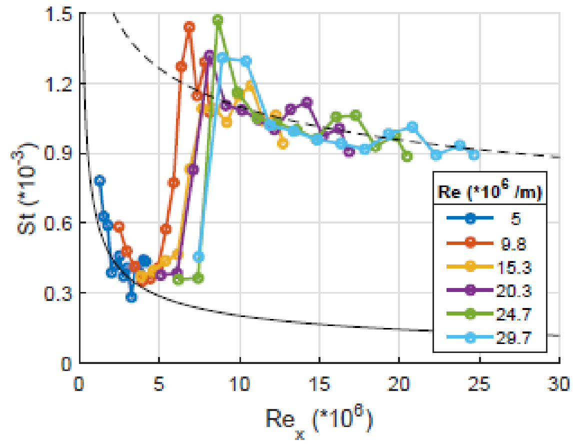

(b) $\beta = 0, \alpha > 0$.

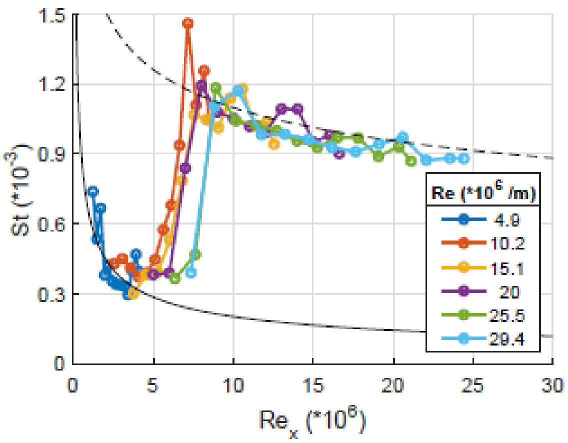

(c) $\alpha = 0, \beta < 0$.

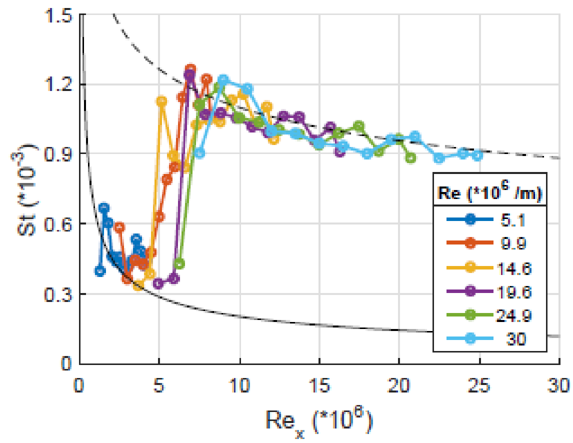

(d) $\alpha = 0, \beta > 0$.

Figure 18 Streamwise non-dimensional heat-flux profile. $\phi = 45°$.

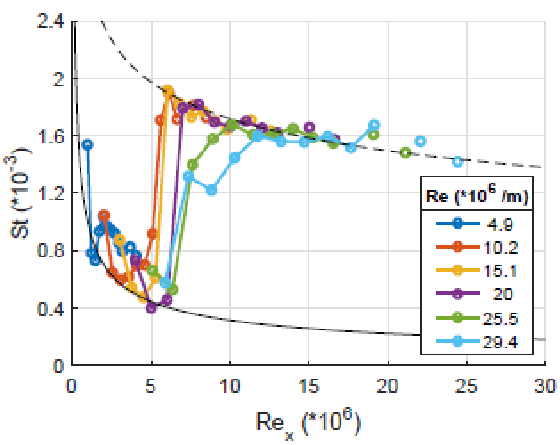

(a) $\alpha = 0, \beta < 0$.

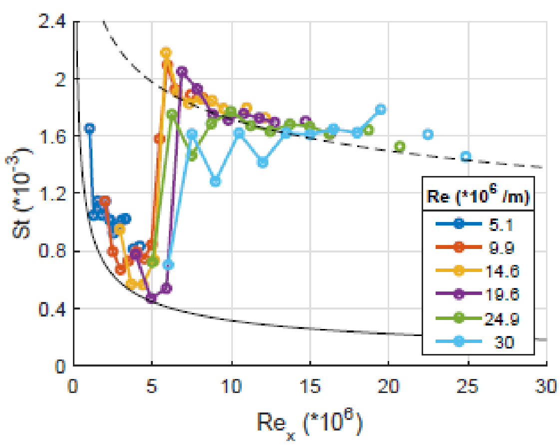

(b) $\alpha = 0, \beta > 0$.

Figure 19 Streamwise non-dimensional heat-flux profile. $\phi = 90°$.

2.5. Transitional Heating Overshoot

Transitional overshoot has been observed numerous times in wind tunnel tests. Overshoot is defined here as an elevation of heating rates above their expected equilibrium turbulent values during the transition process. Overshoot is followed by a relaxation of heating rates to equilibrium turbulent trends. The phenomenon seems to be quite variable and is not fully understood. To determine if overshoot is peculiar to wind tunnels or if it also occurs in flight, the HIFiRE-5b flight data were examined for evidence of overshoot. The process consisted of two steps. First, a qualitative analysis of the data revealed the presence of overshoot. Once this was ascertained, quantitative analysis determined the magnitude of the overshoot.

Traditionally, overshoot is visualized in wind tunnel data by plotting heat transfer as a function of axial location, in the fashion of Figure 14 through Figure 19. Indeed, transitional overshoot does appear to be present, especially along the $\phi = 45$ and 90° rays (Figure 18, Figure 19b). However, the relatively sparse streamwise transducer spacing on HIFiRE-5b and scatter created by noise make it difficult to confidently assess the magnitude of the overshoot. To obtain a denser distribution of heating as a function of Re_x, the heat transfer for numerous transducers at $\phi = 0$, 45, and 90° were plotted as a function of Reynolds number. Figure 20 shows these data for each transducer for x 400 mm. Points nearer to the nose were excluded, since the flow here showed large departures from similarity, and the scaled heating did not collapse with the downstream data. Each data point represents a maximum (positive) or minimum (negative) angle of attack or yaw, and are colored according to the payload orientation. In each plot, the solid line corresponds to the $\alpha = \beta = 0°$ sharp elliptical cone empirical heating correlation described previously.

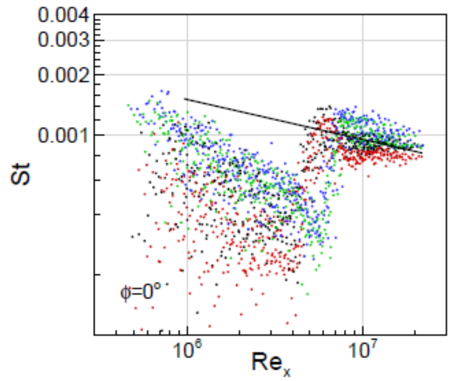

(a) $\phi = 0°$.

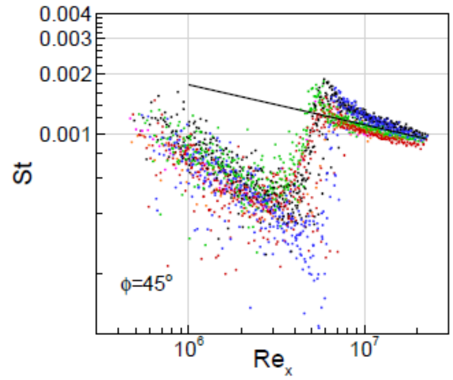

(b) $\phi = 45°$.

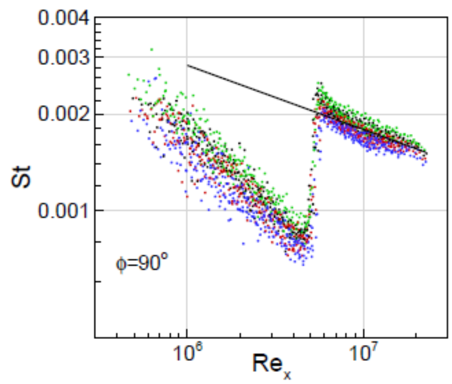

(c) $\phi = 90°$.

Figure 20 Heat transfer coefficient as a function of Reynolds number. Black line – turbulent correlation. Black points - α_{max}, red - α_{min}, green - β_{max}, blue - β_{min}

Clear trends emerge despite the data scatter. The data points, especially for turbulent flow, tend to segregate into distinct bands based on the vehicle attitude. The empirical correlation, a 1/5th power scaling, describes the turbulent data well for high Reynolds number. The $\phi = 0°$ data exhibit wider scatter around this correlation than the other two rays, probably due to a lack of flow field similarity on the centerline ray. The immediately post-transitional data on the $\phi = 45$ and 90° rays do not scale with the 1/5th power trend and overshoot it. In contrast, the $\phi = 0°$ data show no evidence of overshoot. Clearly, transitional overshoot occurred on HIFiRE-5b during flight, but only in limited regions. To determine if overshoot occurred preferentially for some payload attitudes and not others, data from the $\phi = 45°$ ray were segregated into instances of maximum and minimum angle of attack and yaw. Figure 21 shows the $\phi = 45°$ data conditioned on angle of attack and yaw. Clearly, overshoot occurred at all extremes of the vehicle attitude, and vehicle attitude did not systematically affect the presence of overshoot.

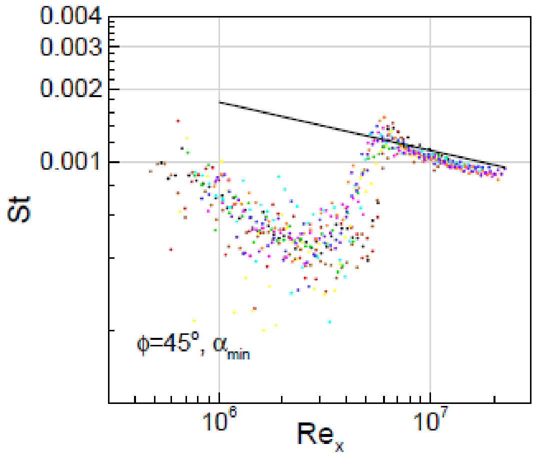

(a) Minimum α.

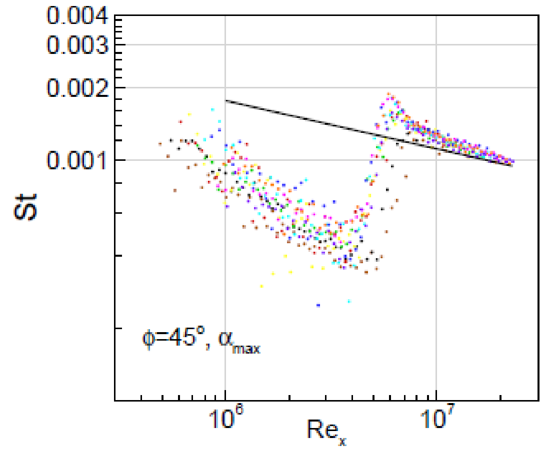

(b) Maximum α.

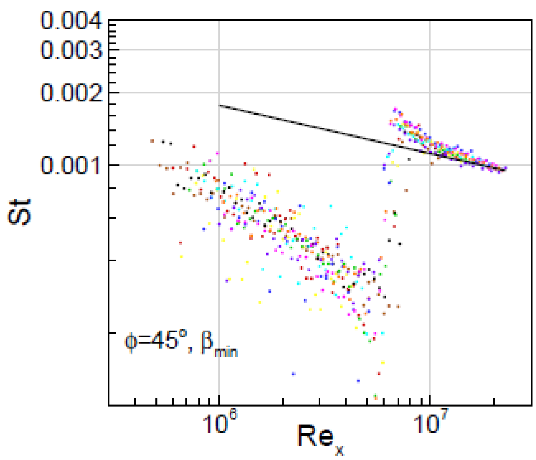

(c) Minimum β.

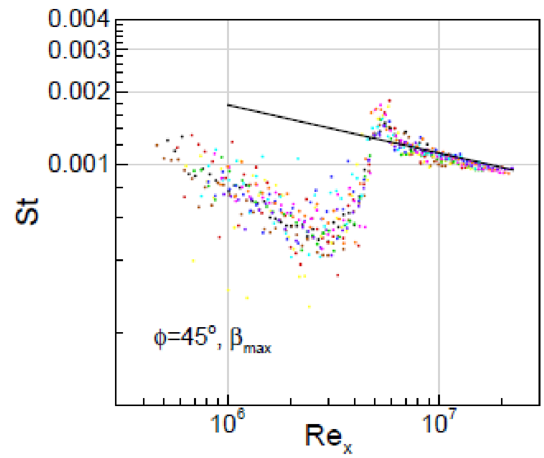

(d) Maximum β.

Figure 21 Heat transfer for $\phi = 45°$ ray conditioned on maximum and minimum angle of attack and yaw.

Having established that turbulent overshoot occurred on the ϕ = 45 and 90° rays, the next step was to quantify the overshoot. Several steps were taken to ensure an unbiased and accurate assessment of the overshoot. First, special care was taken in filtering to ensure that transient transitional heating peaks were not filtered out. To this end, a Parks-McClellan filter [19] was implemented. In this implementation, filter coefficients rolled off linearly between 10 and 20 Hz.

Two additional concerns required that the flight heating data be compared to CFD heating. First, the heating peaks occurred near extrema in the vehicle attitude. Comparing heating peaks in flight data to the $\alpha = \beta = 0°$ empirical correlation would clearly overstate the amount of overshoot. Secondly, the vehicle AoA and yaw, and thus the peak heating associated with these attitude extrema, decreased with time. The concern here was that the apparent overshoots and subsequent decay in heating might simply be due to a decrease in AoA or yaw over time. Since the CFD data had been interpolated to the flight AoA and yaw, comparison of the flight data would obviate this concern. Finally, although heating on the $\phi = 45$ and 90° rays showed reasonably good correlation with a 1/5th power law, assumptions of similarity could be completely avoided by using CFD.

Turbulent heating computations had been executed previously for a variety of vehicle attitudes. These CFD data were interpolated to obtain predicted heating at the measured flight attitudes. The CFD and interpolation process are described in Ref. [10].

A difficulty encountered in using the CFD heating was that, although the computed heating rates generally reproduced the trends and relative fluctuations of the flight data, there was some disparity in the magnitudes of the CFD and flight heating, as noted in Ref. [20]. To account for this, the CFD data were rescaled so as to minimize the RMS differences between the turbulent CFD and flight data for $Re_x \geq 10^7$. Although this resort to scaling was not ideal, the scaled CFD turbulent heating values reproduced the high-Reynolds-number trends of the flight data, as well as the relative heating fluctuations arising from variations in flight vehicle attitude. Figure 22 shows a sample of scaled CFD data compared to flight data for x = 830 mm and $\phi = 90°$.

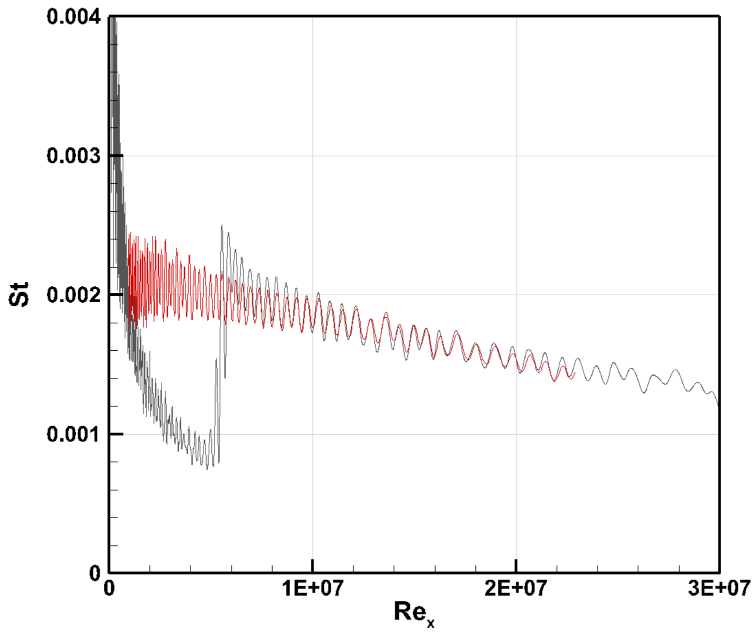

Figure 22 Stanton number for flight data compared to scaled CFD heating.

The magnitude of overshoot was determined by comparing the peak Stanton number from the flight data to the nearest peak in the scaled CFD for x 400 mm along the $\phi = 45$ and 90° rays. The x = 700 and 800 mm stations on the $\phi = 90°$ ray were excluded since the flight data appeared anomalous. Since the $\phi = 0°$ ray exhibited no systematic overshoot, it was not analyzed. The $\phi = 90°$ ray stations showed, on average, a 12% transitional overshoot. The $\phi =$ 45° ray showed a larger overshoot of 26%. Neither ray showed a systematic trend of overshoot with axial location.

The uncertainty in the overshoot estimates was evaluated based on the comparison of the high-Reynolds-number ($Re_x \geq 10^7$) turbulent scaled CFD to the measured flight data. The RMS error between the high-Reynolds measured and computed Stanton numbers was calculated at each station, then averaged over all the stations on a ray. By this measure, the overshoot for the ϕ = 90° ray was 1.12 ± 0.03. For the ϕ = 45° ray, the overshoot was 1.26 ± 0.05.

2.6. Transition Length and Turbulent Spot Generation

Figure 23 through Figure 26 show the locations of transition onset and end when controlling for vehicle attitude. Each subfigure shows data along one of the densely instrumented rays. The transition locations are discrete due to the spacing of the sensors. The distance between the onset and end locations gives the transition length. The normalized transition length is given by the ratio of transition end location to transition onset location, x_{end}/x_{onset}. The determination of onset and end location at a fixed freestream unit Reynolds number is necessarily coarse, because it is limited by the spacing of the thermocouples: 5 cm along the most densely instrumented rays. Sensor spacing was 10 or 20 cm along the other rays, so transition length was not evaluated. This makes evaluation of trends difficult, especially at higher *Re*. However, some are apparent. The transition length is greatest along the ϕ = 0° ray, and least along the ϕ = 90° ray. Although transition location along the centerline was strongly affected by angle of attack, the non-dimensional transition length is not strongly affected (within the uncertainty of the measurement). Similarly, transition length along the leading edges is not strongly influenced by yaw angle. Transition length increases at lower freestream unit Reynolds numbers; both onset and end are of course delayed, but end is delayed proportionally farther. Because these plots of Re_x at transition onset and end at a fixed *Re* are so coarse, calculating Re_x at transition onset and end at a fixed x may be beneficial. Figure 13 in ref. [13] will be the basis for this future analysis. As discussed in Section 2.4.3 , they will be conceptually different from a ground-test or computational result, and will require the implicit acceptance of self-similar boundary layers. This assumption is problematic, considering the indication that transition length does vary with *Re*.

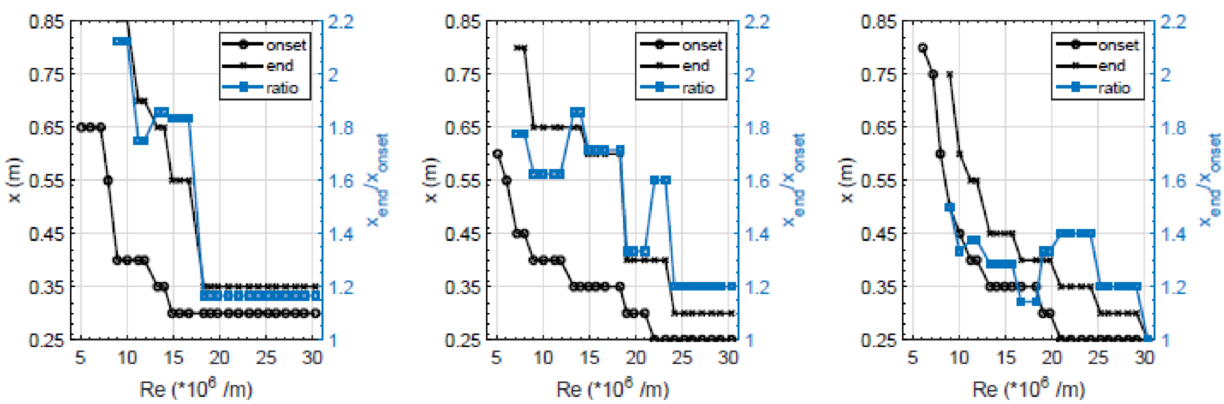

(a) ϕ = 0°. (b) ϕ = 45°. (c) ϕ = 90°.

Figure 23 Transition onset and end locations, α < 0, β = 0.

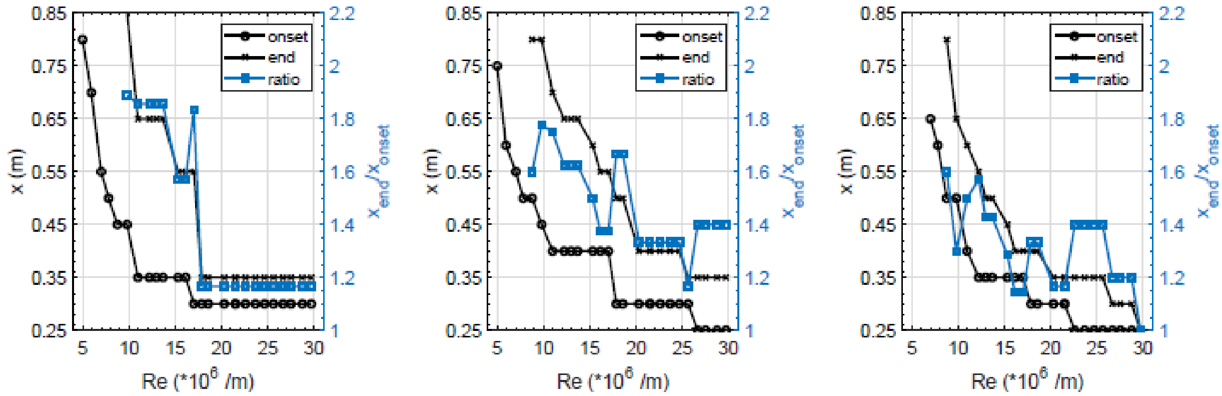

(a) ϕ = 0°. (b) ϕ = 45°. (c) ϕ = 90°.

Figure 24 Transition onset and end locations, $\alpha < 0$, $\beta = 0$.

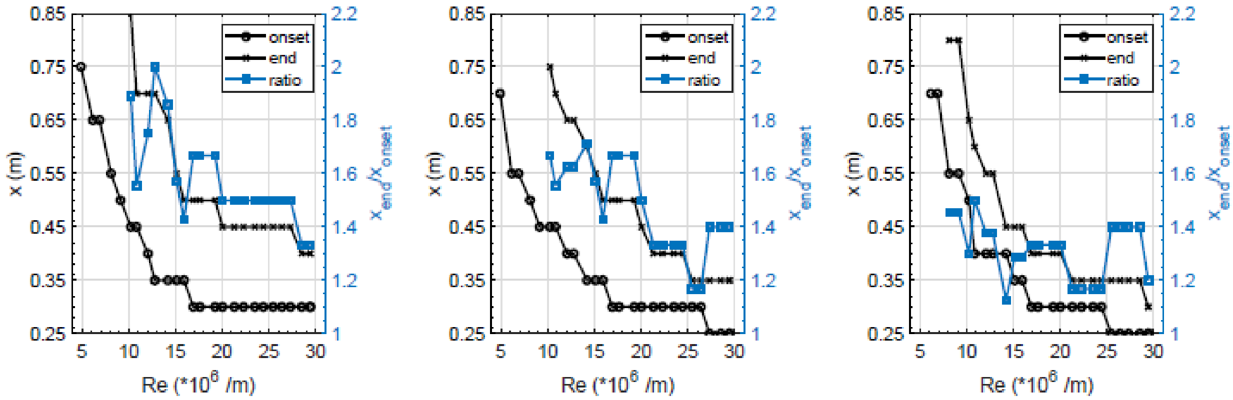

(a) ϕ = 0°. (b) ϕ = 45°. (c) ϕ = 90°.

Figure 25 Transition onset and end locations, $\alpha = 0$, $\beta < 0$.

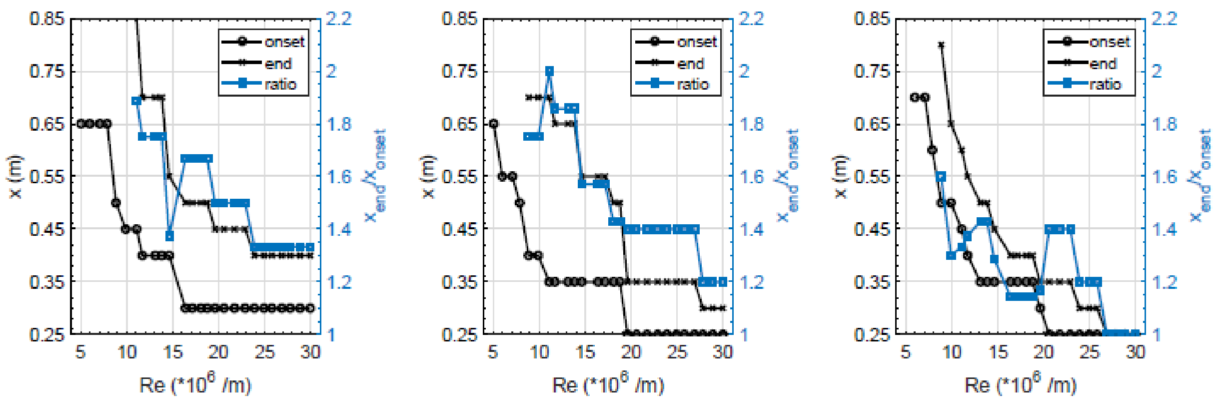

(a) ϕ = 0°. (b) ϕ = 45°. (c) ϕ = 90°.

Figure 26 Transition onset and end locations, $\alpha = 0$, $\beta > 0$.

Jewell et al. [21] used time-resolved and spatially-demarcated heat transfer traces to track the propagation of turbulent bursts, and measured convection rates at approximately 91%, 74%, and 63% of the boundary-layer-edge velocity, respectively, for the leading edge, peak, and trailing edge of the spots. With the measured parameters, a simple stochastic geometric model for the propagation of turbulent spots, following Mee and Tanguy[22], was used to infer turbulent spot generation rates from observed transition onset to completion distance. A similar procedure is implemented for the present flight data, based upon the universal intermittency curve of Narasimha[23,24], where γ is the intermittency, or fraction of the test time that the flow at a given x-displacement beyond the transition onset location, x_{onset}, is turbulent. The universal intermittency curve for axisymmetric conical flow, as derived by Cebeci and Smith[25],

$$\gamma_{cone}(x) = 1 - \exp\left[-\frac{n\sigma}{u_e} x_{onset}\left(\ln\frac{x}{x_{onset}}\right)(x - x_{onset})\right] \tag{2}$$

used to model the distribution of γ, with $\gamma = 0$ for $x \leq x_{onset}$, and $\gamma = 0.99$ taken as $x \approx x_{end}$. The geometry at the $\phi = 0°$, 45°, and 90° thermocouple arrays, where transition is measured, is assumed to be locally similar to an axisymmetric cone with the equivalent half-angle (i.e. 7° at $\phi = 0°$ and 13.8° at $\phi = 90°$), and the Mach number and velocity inflow conditions are adjusted from the best estimated trajectory based upon this assumption.

The relationship between γ and x in Eq. 2 depends upon edge velocity, the nondimensional spot growth (or propagation) parameter σ of [26], and the spot generation parameter n, which is the number of spots generated per unit length and time across $x = x_{onset}$. σ incorporates both lateral and streamwise growth, and is commonly taken to be,

$$\sigma = \left[\frac{1}{C_{te}} - \frac{1}{C_{le}}\right]\tan\vartheta \tag{3}$$

as in ref. [27]. Both c_{le} and c_{te} are velocities nondimensionalized by u_e. As c_{le} tends to be larger than c_{te}, the spot grows longitudinally as it progresses downstream. The rate at which it grows laterally is controlled by ϑ and the local angle of the cone. The spreading angle is assumed to vary inversely with edge Mach number for each case with the theoretical relationship found by Doorley and Smith [28], $\vartheta = 3^{-3/2}\sqrt{2}M_e$. Figure 27 presents the turbulent spot generation rates inferred from the transition onset to completion distances recorded in Figure 23 through Figure 26. The uncertainty bars placed on every fifth data point are calculated from the model uncertainty in turbulent spot leading- and trailing-edge propagation rates, which is estimated as 0.03 for both parameters, following observations reported in ref. [21]. As the time resolution of the HIFiRE-5b flight sensors does not allow for the direct observation of individual turbulent spots in the flight data, the reliability of this assumption is unknown. In all cases, the spot generation parameter n increases with increasing unit Reynolds number, which was also observed in the reflected shock tunnel transition data examined by Mee and Tanguy[22]. The inferred spot generation rates along each ray of thermocouples also approximately agrees, for similar unit Reynolds numbers up to 10×10^6 /m, with results reported in [21]. While these previous results spanned a much smaller range in unit Reynolds number, similar turbulent spot generation rates of $n = 5–10 \times 10^6$ spots/m/s are observed in the present data at unit Reynolds numbers lower than 10×10^6 /m. The largest n values are achieved at lower unit Reynolds numbers for the $\phi = 90°$ leading edge case than for either the $\phi = 0°$ or 45° cases. With the exception of the cases in Figure 27, for the $\phi = 0°$ center line ray, similar n progression with unit Reynolds number is inferred for each of the four sub-sampled data sets. This may indicate that a different transition, or spot-generation, mechanism is important for the un-yawed $\beta = 0$ sub-sampled data sets along the $\phi = 0°$ sensor ray than for the two yawed $\alpha = 0$ sub-sampled data sets, which have lower inferred n for similar unit Reynolds number.

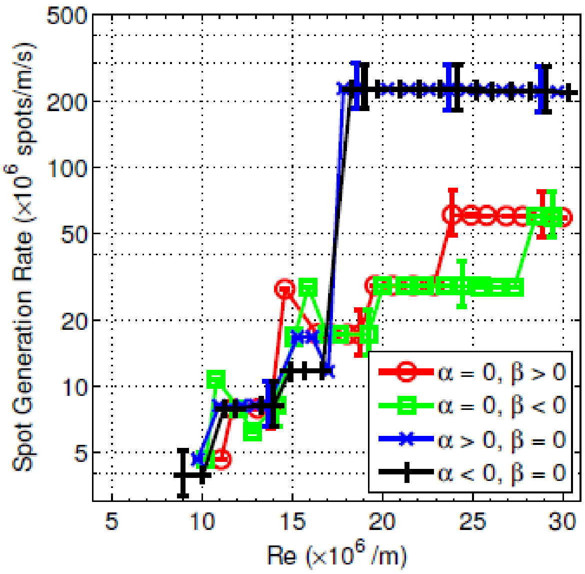

(a) $\phi = 0°$.

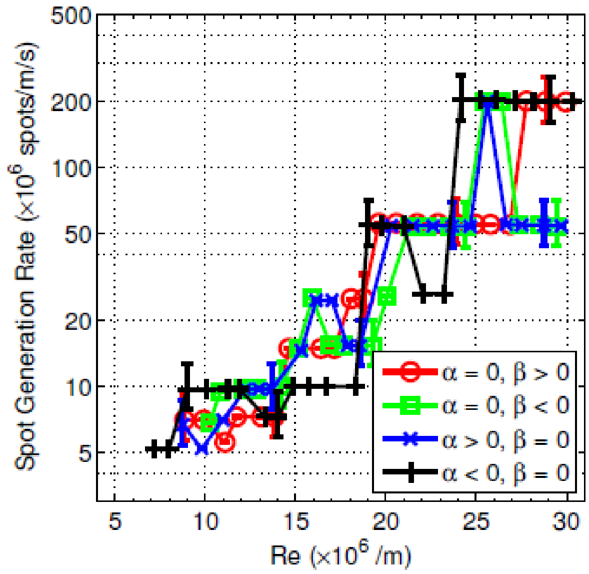

(b) $\phi = 45°$.

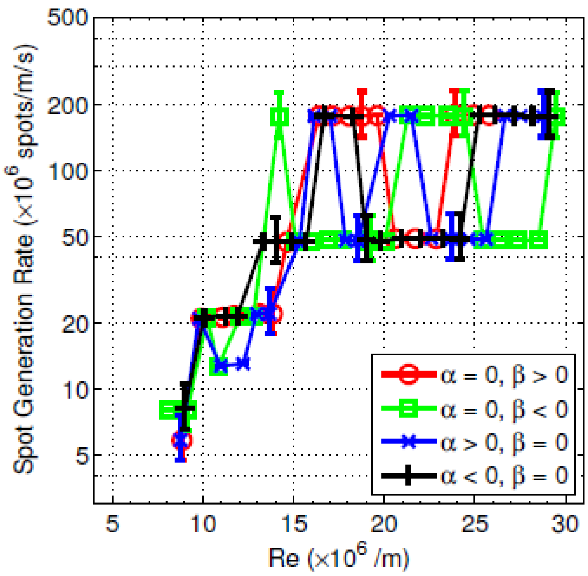

(c) $\phi = 90°$.

Figure 27 Inferred turbulent spot generation rates n with varying unit Reynolds number.

2.7. Section 2 Conclusions

The successful HIFiRE-5b hypersonic flight test provided a wealth of surface-temperature data, from which heat flux was calculated and boundary-layer transition was derived. A three-lobed transition front was observed, with transition onset farthest forward near the centerline, along the leading edges, and part way in between. Three different instability mechanisms are suspected as the causes of boundary-layer transition: inviscid instability near the centerline, where the boundary-layer velocity profile has an inflection point, second-mode waves at the leading edges, and crossflow instability in between.

Correlating pressure-transducer data with CFD analysis has been found to be effective for determining angle of attack and yaw. Their effects on heat transfer and boundary-layer transition have been isolated by sub-sampling the data. Controlling for vehicle attitude significantly reduced heat-flux fluctuations. Heating rates measured across a plane of symmetry exhibited a difference within the uncertainty expected for this instrumentation. The time-varying heat-flux was separated into slowly varying and oscillating components. The difference between the mean heating experienced by sensors on opposite sides of the vehicle is on the order of the uncertainty estimated in the temperature measurement and calculation of heat flux. Correlating the oscillating component of heat flux with yaw angle permitted calculation of the sensitivity of heat flux to yaw angle for sensors along the leading edges. This analysis also pointed toward an optimal filter duration for the thermocouple signals; a 10 ms moving average was found to reduce noise without significantly sacrificing sensitivity.

The data from multiple sensors have been combined into profiles more akin to conventional presentation of ground-test and computational results. These profiles show the expected trend of heat flux and transition dependence on freestream unit Reynolds number. Indeed, laminar and turbulent heating rates collapsed substantially when non-dimensionalized and largely followed a relatively simple empirical predictions.

Transitional heating overshoot occurred on HIFiRE-5b during flight, but not uniformly over its surface. It was observed on the $\phi = 45$ and 90° rays, but not the $\phi = 0°$ ray. The $\phi = 90°$ ray stations showed, on average, a 12% transitional overshoot, whereas the $\phi = 45°$ ray showed a larger overshoot of 26%. Although the cause of transitional heating overshoot could not be determined, it can be confidently stated that it is not an artifact of freestream noise level, wall-to-stagnation temperature ratio, or some other aspect of ground-test experimentation.

Transition length was examined, subject to the constraints of sensor spacing for a flight-test vehicle. It was shorter on the leading edges, longer along the centerline, and dependent upon freestream Reynolds number. Transition onset location and length were also used to calculate the turbulent spot generation rate. Connecting the model of spot generation to the pressure fluctuations measured in flight remains as future work.

3. Implicit Large-Eddy Simulation of Discrete Roughness Boundary-Layer Transition with Added Perturbations

3.1. Introduction and motivation

A key enabling technology in the development and implementation of hypersonic flight vehicles is an accurate method of predicting, or at least bounding, the location where the boundary layer will undergo transition to turbulence. For example, Anderson [29] cites a study wherein the choice of criterion for transition Reynolds number caused a mass change in the final vehicle design of up to 50%. In many external aerodynamics applications, the process of the boundary-layer naturally transitioning to turbulence consists of several stages. In the first stage, environmental disturbances combine with geometric and flow features of the given geometry to introduce disturbances into the boundary layer. These disturbances are selectively amplified by the flow until reaching some critical amplitude, which in turn triggers parametric instabilities and nonlinear interactions leading to breakdown and turbulence. This is summarized by Path "A" in the ubiquitous "Pathways to Turbulence" illustration, here Figure 28, first presented by Morkovin et al. [30]

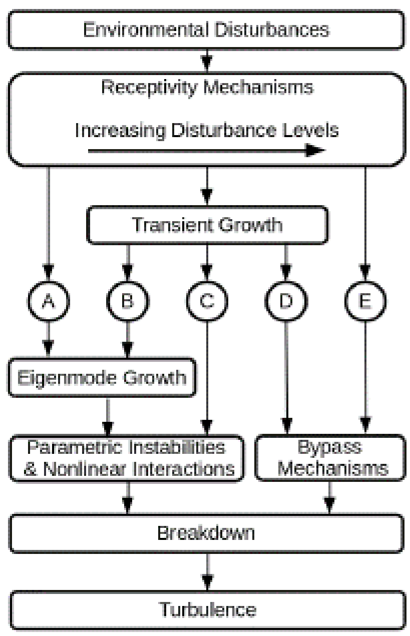

Figure 28 Pathways to Turbulence in Wall Layers

In certain cases, methods based on the Parabolized Stability Equations (PSE) have been shown to provide a reasonable estimate of boundary-layer transition. [31] However, the assumptions inherent in PSE render these methods ill-suited to analysis of many complex flows. Even in relatively simple geometries such as a yawed circular cone or an elliptic cone, there exist regions in the flowfield that are unable to be easily tackled using conventional PSE due to spanwise in-homogeneity. In addition, PSE and similar methods based on a growth criterion (e.g., "e^N" [32]) do not directly model environmental disturbances, receptivity mechanisms nor breakdown to turbulence. In such methods, these phenomena are accounted for only in the empirical correlation present in the choice of transition N-Factor. Only Nonlinear-PSE (NPSE) methods model transient growth, parametric instabilities and nonlinear interactions. In addition, PSE are not suited to modeling any of the bypass mechanisms to turbulence.

A key point in Figure 28 and related discussion is that transition to turbulence is an initial-value problem predicated on conditions present in the combination of environmental disturbances and geometric features (receptivity). Beyond an effect of amplitude of growth or location of transition, in some cases even the fundamental mechanisms governing transition to turbulence can be modified by differences in these parameters. In the context of paths to turbulence, this may change the primary eigenmodes responsible for transition (e.g. traveling vs stationary crossflow) or even change the path to transition (e.g., from "A" to "C" in Figure 28)

In addition, neither the freestream disturbances present in hypersonic wind tunnels nor those in the atmospheric freestream are fully characterized, since to do so requires specification of more than a freestream turbulence amplitude. Full characterization implies specification of amplitudes, frequencies, length scales, and orientation of both acoustic and vortical disturbances. [33] Therefore, to fully understand the process of the boundary-layer transitioning to turbulence studies including receptivity and breakdown are needed.

With recent increases in computational power and efficiency, DNS studies are becoming increasingly useful tools for the study of transition because of the ability to examine receptivity effects. Malik et al. [34] performed studies investigating receptivity over a sharp wedge. In this case, it was seen that forcing with planar acoustic waves, a suction/blowing slot, and with free-stream Mach waves all resulted in the same instabilities emerging in the boundary layer. Ma and Zhong [35] studied the same geometry as Malik et al., [36] and perturbed with various different free-stream forcing types. Ma and Zhong concluded that the stable modes in the boundary layer affected receptivity. Wang et al. [37] for the same wedge geometry showed that the location of wall blowing/suction relative to the synchronization point of fast and slow modes strongly affects the receptivity to this perturbation. Upstream of the synchronization point slow modes are strongly amplified, however downstream of this point there is little amplification. Balakumar [38] found that isolated two-dimensional roughnesses do not contribute much in the way of disturbance generation when subjected to acoustical freestream disturbances.

Fong et al. [39, 40] were able to predict and demonstrate experimentally that judiciously placed roughness elements are able to damp out Mack 2nd Mode disturbances in the boundary layer. This effect appears to be largely due to mean flow modifications, as Linear Stability Theory (LST) is capable of capturing this particular effect despite the assumptions present in the derivation of LST (parallel flow, spanwise homogeneity).

Gronvall et al. [41, 42] showed that DNS of small-scale distributed surface roughness features on a 7◦ half-angle yawed cone was able to successfully seed the stationary crossflow instability, and simulate the growth of this instability. Neither study, however, made observations on the secondary instabilities or breakdown to turbulence as the resolution was insufficient to capture these effects. [42]

Gronvall et al. [43] performed both steady and unsteady high-order simulations of a discrete roughness element on the full scale HIFiRE-1 vehicle. Gronvall et al. showed that when using unsteady low-dissipation schemes, high-order simulations are able to capture breakdown to turbulence and the resulting increased heating due to discrete roughness elements.

More recently, Hader and Fasel [44, 45] utilized direct numerical simulations of transition and breakdown to turbulence on a flared cone geometry to examine a peculiar heating pattern seen experimentally under quiet wind- tunnel conditions. Hader and Fasel [44] were able to use random forcing of the boundary layer and obtained results similar to experimentally observed behavior.

It was suggested by Saric et al. [46] that the role of freestream disturbances, particularly in the case of roughness-induced effects, should be re-examined with DNS studies. In addition it has been demonstrated by the results summarized by Saric et al. that until the details of receptivity are better understood, experiments performed on surrogate geometries do not provide the entire picture. Therefore, it is desirable to perform these types of detailed transition studies on realistic, rather than surrogate, geometries. [46]

Tufts et al. [47] simulated tripped transition to turbulence without external forcing using an ILES methodology. This section is a continuation of that work, with the addition of the simulations including the additional perturbations to the flowfield

3.2. Reference Experiment

3.2.1. Model Geometry

The conditions and geometry are selected to represent the conditions published by Casper et al. [48] The baseline model geometry is a 7◦ half angle cone, with a spherically blunted tip of radius 1.19 mm. A summary of the geometric conditions can be found in Table 3.

Table 3 Model Geometric Dimensions

Half Angle	Nose Radius [mm]	Base Radius [mm]	Overall Length [mm]	Trip Location [mm]
7°	1.19	120.0	405	130.0

The experimental series also included a boundary-layer trip of varying heights located at 0.32 *x/L* relative to the cone; 130 mm from the nosetip. Following Casper et al., the trips in the computational model are a 1.27 mm by 1.27 mm square planform of varying heights with one corner facing the streamwise direction. The present results use a boundary-layer trip that is perfectly "sharp" (not rounded) on all corners and edges. In both the experiment and computations the trip is located on the windward ray when the cone is yawed. The cone's surface, with the exception of the boundary-layer trip, is assumed to be perfectly smooth in the computational model.

3.2.2. Free Stream Conditions

Freestream conditions in the reference experiment were those as experienced in the BAM6QT installed at Purdue University. The cone was tested at Mach 6, with unit Reynolds numbers approximately 8.7×10^6 per meter. Flow conditions included two angles of attack, and also included both quiet (low-disturbance, noise levels ≈ 0.05%) and noisy (high disturbance, noise levels ≈ 2-4.5%) flow conditions. Computationally, a subset of the trip heights studied by Casper et al. were simulated.

Because of the relatively short test times in the BAM6QT facility, all simulations assume a no-slip, uniform temperature, isothermal wall boundary condition where T_w = 300 K.

3.3. Computational Methods

3.3.1. Solution Method

Solutions are calculated using Overflow 2.2n. [49] The grid Overset/Chimera grid system was developed using an in-house circular cone grid generation tool. In order to achieve favorable load balancing, the max grid size was limited to be O(100M pts), and the resulting cone grid system was developed with a total of 9 grids (including 3 grids to define the trip). PEGASUS 5 grid tools [50] were used to determine connectivity and hole cutting. For the entire grid system, at least 5 pt overlaps were maintained.

An overview of the surface geometry is seen in Figure 29a. For reference, the location of the trip is shown in red, and the location where perturbations are introduced into the flow is shown as a blue line.

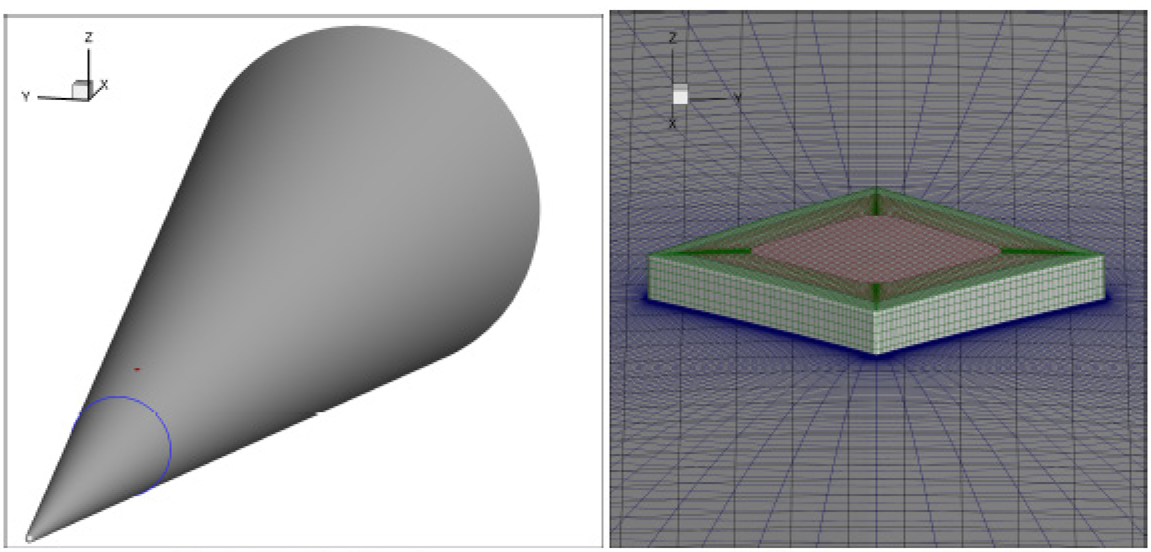

a) Surface Topology Overview b) Grid Topology around Discrete Trip

Figure 29 Surface Geometry

The grid system maintains a y^+ of less than one on all surfaces, meaning that the smallest scales in the wall-normal direction are fully resolved at the surface. The wall-normal spacing at the wall was 7.60 x 10^{-3} mm at the trip location, growing to a maximum spacing of 0.5 mm outside the shock. The grid distribution has approximately 50 points within the boundary layer at the trip location, and a maximum y^+ on the order of 100 in the boundary layer. 243 total wall-normal points are used. Streamwise/spanwise spacing at the cone surface ranged from 1.27×10^{-2} mm to 5.15×10^{-1} mm, resulting in a maximum Δx^+ and Δz^+ on the order of 15. The complete grid system has 511 million nodes, for a full cone, though note that not all grid points are solved on due to hole cutting. Grid resolution figures are given in Table 4, where "*i*" is nominally streamwise, "*j*" is nominally wall-normal, and "*k*" is nominally in the azimuthal direction.

Table 4 Overflow Grid Dimensions (Production Grid)

Grid Name	i	j	k	Grid Type
Nose Cap Grid	123	243	121	Cap Grid
Cone Grid 1	1338	243	491	O-Grid
Cone Grid 2	1115	243	491	O-Grid
Shock Cap Grid	246	31	245	Cap Grid
Shock Grid 1	2532	31	983	O-Grid
Shock Grid 2	950	31	4899	O-Grid
Trip Capture Grid 1	41	41	72	Cap Grid
Trip Capture Grid 2	197	21	100	O-Grid
Trip Capture Grid 3	197	97	Varies ($\approx \frac{k}{0.01\,mm}$)	O-Grid

Trip grids were creating using an in-house script based on the Chimera Grid Tools program. The surface of the trip is captured with three grids, as was done in Tufts et al. [47] An inset image of these grids can be seen in Figure 29b. The first grid is a Cartesian "cap" grid transitioning the grid into the main-body grid. (Red in Figure 29b) The second grid captures the top corners of the trip which transition from the sides to the top of the grid. (Green in Figure 29b) The final grid is an O-grid surrounding the planform of the grid and is extruded wall-normal, capturing the meeting of the trip with the cone's surface. (Blue in Figure 29b) Note that the final grid (Trip Capture Grid 3) varies in the *k* dimension in order to produce the height of trip needed, but the spacing is approximately 0.01 mm for all cases. The cone-surface grid visible in Figure 29b is shown in black.

All results are run using 5th order WENO spatial discretization using the van Albada flux limiter with 2nd order implicit time-stepping. Fluxes were computed using the HLLC upwind scheme, and solved with SSOR using 10 subiterations. The time step taken is constant, at 1.45×10^{-8} sec/iteration. Time-averaged data and spectra were computed over a total flow time of 1.09×10^{-3} seconds.

3.3.2. Grid Resolution Studies

Sensitivity to grid resolution was examined by plotting heating coefficients for three different grid systems. A coarse grid was made by coarsening the production grid system by a factor of 0.8 in all directions. A fine grid was made by refining a 30° wedge of the cone's surface surrounding the trip from x = 120 mm to the end of the cone by a factor of 2 in both of the wall-tangential directions. The refined region is visible in Figure 30c as a black outline. Due to computational costs, the wall-normal direction was not refined as part of the grid sensitivity study.

Grid resolution studies were calculated using the 0° AoA flow conditions without added disturbances. Contours of instantaneous coefficients of surface heating for the three grid levels are visible in Figure 30. It can be seen from Figure 30 that the development of the instabilities leading to transition is similar for all three cases. The details of the transition process and post-breakdown heating levels are somewhat sensitive to the grid resolution. The transition location (start of breakdown) based on the start of increased heating occurs 13% earlier for the fine case.

In addition, the fine grid, visible in Figure 30, appears to shed "packets" of turbulence over the last 100 mm of the cone, while the two coarser grids do not. This indicates that the production grid is not fully converged in terms of spatial resolution. However, the development of the disturbances appears similar between the grids, so examination of the relative effects of the trips and disturbance levels is thought to be acceptable with the production grid while significantly reducing the computational expense.

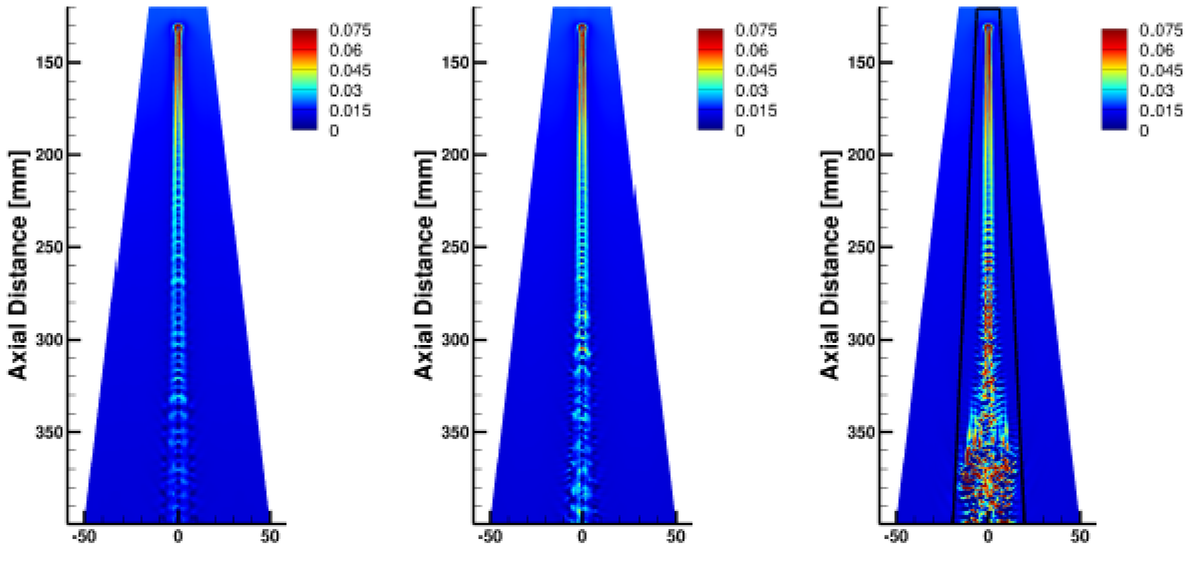

a) Coarse Grid

b) Production Grid

c) Fine Grid
(Refined Region Outlined in Black)

Figure 30 Instantaneous Coefficient of Heating, k = 0.89 mm, 0° AoA, $p_{rms} \approx$ 0.00%

3.3.3. Generation of Perturbations

Perturbations introduced are a linear superposition of procedurally generated planar acoustic waves of a form similar to those in Ma & Zhong [35] and Cerminara et al. [51] Note that the equations have been reformulated relative to these references in order to conform with the non-dimensionalizations used by Overflow.

A given seed number is used to pseudo-randomly generate several matrices containing amplitudes and wave propagation angles relative to the freestream. This procedure gives an analytic function in three-dimensional space that defines the disturbances. Because the disturbances are procedurally generated using the same seed number, adjustments to the amplitudes are decoupled from adjustments to the wavelengths, and a given disturbance field is repeatable both between runs of the same grid and between grids of different resolutions or different trip heights. Creating the disturbances in this manner also means the disturbances are continuous across chimera-grid boundaries and overlaps.

The disturbances are generated with five matrices, $A_{i,j}$, $\Theta^1_{i,j}$, $\Theta^2_{i,j}$, $\Phi_{i,j}$ and $K_{i,j}$ defined as follows.

$A_{i,j}$ is a normal, random distribution from [0,1] that is then scaled so that the L2 norm of all perturbation strengths $\sqrt{\sum_{i=1}^{N}\sum_{j=1}^{N} A_{i,j}^2}$ is equal to an overall strength set in the input deck

$\Theta_{i,j}^1$, $\Theta_{i,j}^2$, and $\Phi_{i,j}$ are all uniform, random distributions from [$-\pi$, π] radians

$K_{i,j}$ is the linearly spaced progression from the smallest length scale set in the input deck to the largest.

Having set all these matrices, for any given wave (i, j) we can draw five amplitude and propagation vector parameters: $k=K_{i,j}$; $\theta_1 = \Theta_{i,j}^1$, $\theta_2 = \Theta_{i,j}^2$, $\varepsilon=A_{i,j}$, and $\phi = \Phi_{i,j}$. The subscripts i and j define a wave of a given wavelength set with i having j orientations. For the current results both i and j spanned [1; 50] giving 50 wavelength "bins" containing 50 orientations each.

Knowing the wavenumber of the wave allows us to set the frequency

$$\omega = \frac{2\pi}{k}\left(V^* - a^* \sin(\theta_1)\sin(\theta_2)\right) \tag{4}$$

We can also define a wave propagation vector $\bar{x}$

$$\bar{x} = \sin(\theta_1)(x\sin(\theta_2) + y\cos(\theta_2)) + z\cos(\theta_1) \tag{5}$$

which, in turn, allows the definition of the perturbation

$$\begin{Bmatrix} \rho' \\ u' \\ v' \\ w' \\ e' \end{Bmatrix} = \begin{Bmatrix} \rho' \\ u' \\ v' \\ w' \\ e' \end{Bmatrix} \cos\left(\frac{2\pi}{k}\bar{x} + \omega t + \phi\right) \tag{6}$$

$$|\rho'| = \varepsilon$$

$$|u'| = \varepsilon \sin(\theta_1)\sin(\theta_2)$$

$$|v'| = \varepsilon \sin(\theta_1)\sin(\theta_2)$$

$$|w'| = \varepsilon \cos(\theta_1)$$

$$|e'| = \frac{1}{\gamma}\varepsilon$$

The disturbances are then introduced computationally via a right hand side source term in the solution. Note that because the matrices $\Theta_{i,j}^1$ and $\Theta_{i,j}^2$ range between [$-\pi$, π] the disturbance field will contain both "fast" and "slow" acoustic waves at any number of oblique angles relative to the surface.

In the current results, perturbations are introduced at an axial location of 110 mm (20 mm upstream of trip) in a single annular ring surrounding the entire circumference of the cone. This annulus extends from the wall to approximately 2 times the boundary layer thickness, well below the height of the shock. According to stability theory results for these conditions the 1st neutral point for 2nd mode waves occurs at x = 90 mm, thus the perturbations are introduced approximately halfway between the first neutral point and the trip location. Perturbations were inserted at this position to avoid necessitating a grid system fine enough to both fully resolve the bow shock and the perturbations passing through it, and because the alternative shock-fitting boundary conditions as used by Ma & Zhong [35] are not implemented in Overflow. The range of wavelengths included in the perturbations included were 0.381 mm to 2.54 mm, resulting in a perturbed spectrum centered at 350 kHz, as can be seen in the x = 126 mm trace in both Figure 31a and Figure 31b. Note 126 mm is aft of the location where the perturbations are inserted (110 mm) and upstream of the trip (130 mm). Figure 31 is produced from surface pressure fluctuations sampled along the surface of the cone at the indicated axial location.

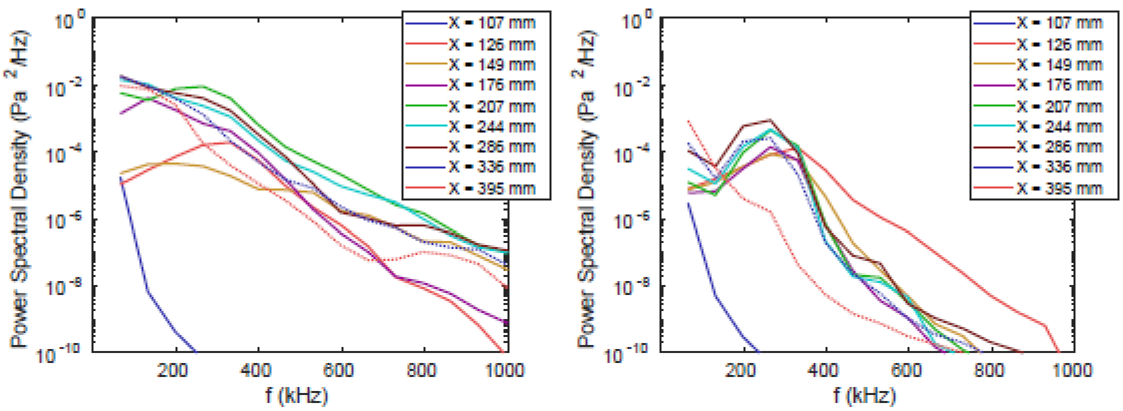

a) Windside (Wake of Trip, Trip at x = 130 mm) b) Leeside (No Trip)

Figure 31 Power Spectral Density, Surface Pressure Fluctuations, k=0.71 mm, 0° AoA, p_{rms} ≈ 0.18%

Fluctuating pressure levels of the input forcing (p_{rms}) were characterized by sampling pressure traces approximately 10 mm aft of the perturbed location at about one boundary-layer thickness (0.5 mm) off the surface of the cone. The fluctuation level is reported as $p_{rms} = \mathrm{rms}\left(\frac{p'}{\bar{p}}\right)$ where p' is the fluctuating value of pressure and $\bar{p}$ is the mean value of pressure. This value of p_{rms} characterizes the fluctuation levels, but is not directly comparable to the freestream fluctuation levels reported experimentally, here denoted as $pitot_{rms}$. Experimental freestream fluctuation levels were measured via the insertion of a pitot probe into the flow of the wind tunnel, and $pitot_{rms}$ is calculated from the measured stagnation pressures as $\mathrm{rms}\left(\frac{p_0'}{\bar{p}_0}\right)$. Pitot-probe measurements taken in hypersonic flows introduce interactions between the disturbances being measured and the probe itself, resulting in a non-uniform transfer function between the disturbances in the freestream and the measurements being taken by the probe. This transfer function is dependent upon the orientation of the disturbance waves to the probe, Reynolds number of the flow, frequency of the disturbance, pitot probe geometry, and potentially other factors. For this reason, direct comparison of the two quantities is not possible without further investigation. Further discussion on this topic can be found in Chaudhry and Candler [52] and Chaudhry et al. [53]

Note also that the computationally introduced perturbations contain only planar acoustic waves, which are inserted behind/inside the shock created by the cone. It has been shown by Fedorov [54] and Ma and Zhong [35] that because any freestream disturbance must be processed by the shock, experimental geometries are likely to experience acoustic waves, entropy waves, and vortical disturbances regardless of what is contained in the freestream. Therefore, the current computational cases do not contain all types of disturbances present in experimental data. Previous work [47] established that the shear-layer caused by the wake appears to be leading to transition behind the trip. The types of freestream disturbances most suited to causing transition in this shear layer has not been established.

3.4. Computations Without Added Perturbations

3.4.1. Instantaneous Heating Contours

Several cases without added perturbations were calculated using various trip heights and two angles of attack. Computations are generally unable to sustain steady, laminar flow when an absolute instability is present in the flow as absolute instabilities are self-sustaining. Therefore, because a case without perturbation is laminar and steady with larger than the experimentally observed critical height, the computational results suggest that the experimental observation is not that of an absolute instability, but rather of a receptivity source for a convective instability, thus further motivating studies using introduced perturbations.

Taken as a trend, the computationally observed transition locations indicate, as would be expected, that the unmodified computational environment though not “perfectly” quiescent possesses an overall lower disturbance level than a quiet wind tunnel.

Shown in Figure 32 are instantaneous surface heating coefficients for 0° AoA with no added perturbations for four trip heights. The coefficient c_h is here defined as the wall-heating rate normalized by the freestream density times the freestream speed of sound cubed: $c_h \equiv \frac{\dot{q}''}{\rho_\infty a_\infty^3}$. As can be seen in Figure 32, only cases with trip height k = 0.89 mm or larger than appear to transition to turbulence. Note that the contours seen in Figure 32 are instantaneous as opposed to averaged quantities as would be seen in an infrared image, e.g., as was done in Casper et al. [48]. The alternating light and dark patches seen roughly from 215 mm to 265 mm in the k = 0.89 mm case are the footprint of a traveling wave in the wake. Aft of about 265 mm, the small scale features visible in the k = 0.89 figure are indicative of transitional or turbulent flow.

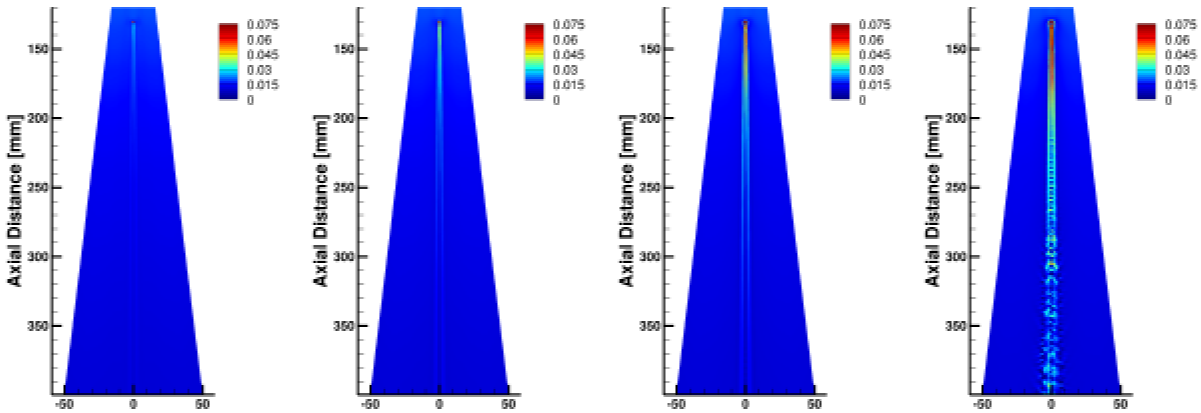

a) k = 0.36 mm   b) k = 0.53 mm   c) k = 0.71 mm   d) k = 0.89 mm

Figure 32 Instantaneous Surface Heating Coefficient, 0° AoA, p_{rms} ≈ 0.00%

3.4.2. Transition Location Trends

Following the form of Casper et al. [48] one may plot the approximate transitional location as a function of roughness Reynolds number ($Re_{kk} = (U_k \rho_k k)/\mu_k$), vs transition location in terms of distance along the cone's axis (X_{Tr}). These values and trend lines for the noisy and quiet flow experimental data from Casper et al. [48] as well as the computational data are plotted in Figure 33. Note that if transition did not occur on the cone as modeled, the transition location is annotated with an upward-pointing arrow, indicating transition would occur at some larger value of x. It is worth noting that the experimental data are derived from infrared images of the cone, which effectively show the averaged heat transfer rates over the cone. Computational transitional locations are derived by examining time-averaged values of heat-transfer on the surface of the cone and selecting the point where heat transfer begins to show a substantial increase rather than monotonically decrease as is observed for the laminar baseline cases.

Similar qualitative trends are seen between the computational data and the experimental data. At low values of the roughness height, despite the visible presence of a wake following the roughness, there is no effect on the transition location as the cone remains laminar over its full length. However, at some height a transition front emerges on the cone, and continues to march forward with increasing height of the roughness. For the experimental data, there appears to be a height above which no further decrease in laminar run length is achieved (the "fully effective" trip height). Computationally, it has not been confirmed if this height has been reached, as further studies with larger trips are needed. However, the expected trend for this case holds. Namely, the noisy experimental cases transition at a lower X_{Tr} for a given Re_{kk} than the quiet experimental cases, which transition at a lower X_{Tr} than the computational cases. This observation holds even for trips that are fully effective.

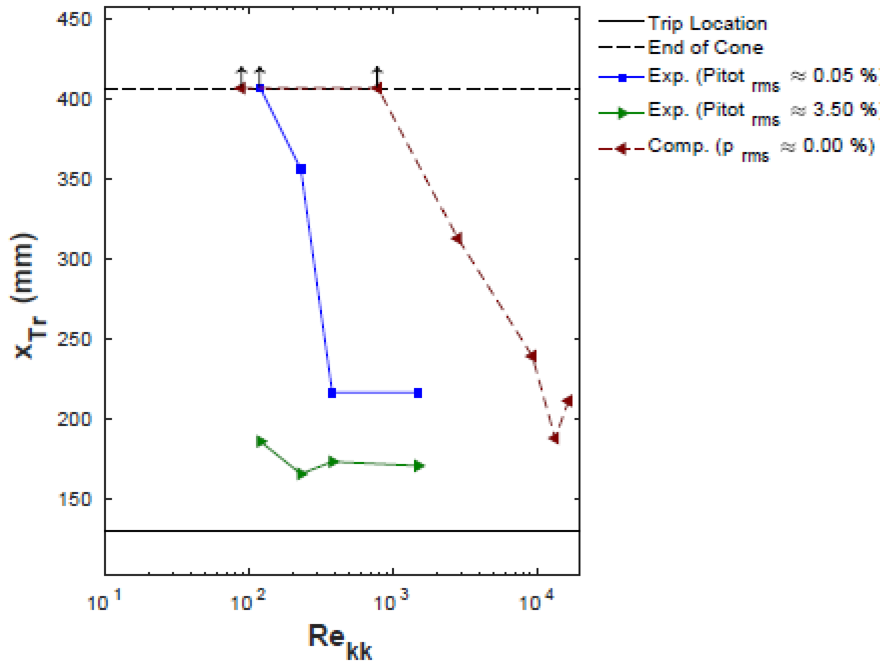

a) 0° AoA

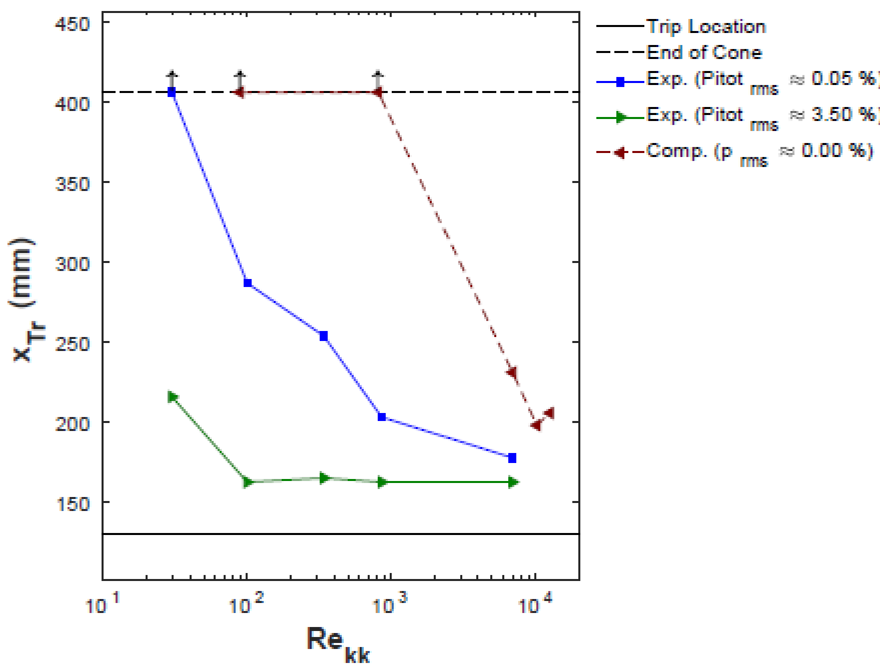

b) 6° AoA, Roughness Windward

Figure 33 Transition Curves, No Added Perturbation

3.5. Computational Results With Added Perturbations

3.5.1. 0° Angle of Attack

Contours of instantaneous surface heating coefficient ($c_h \equiv \frac{\dot{q}''}{\rho_\infty a_\infty^3}$) for perturbation strengths of p_{rms} = 0.09%, p_{rms} = 0.18% and p_{rms} = 0.94% are shown in Figure 34, Figure 35, and Figure 36 respectively. For most cases, the most immediately observable change in the surface heating is the presence of Mack's 2nd mode waves on the surface of the cone. Footprints of the 2nd mode waves are visible outside the trip's wake as alternating light and dark lines oriented normal to the cone's axis. A side-view of pressure contours can be seen in Figure 37, illustrating that the light and dark lines visible on the surface are indeed 2nd mode disturbances as the shape of the disturbances follows that of 2nd mode. Note that for Figure 37 the bottom of the figure represents the wall and flow is from left to right. The 2nd mode waves become stronger and increasingly visible on the surface with higher levels of perturbations. Although the waves grow in strength as they progress down the cone, the waves do not appear to grow as strongly as would be expected from stability theory. For these flow conditions the 2nd mode envelope (with the initial amplitude taken at 110 mm) reaches a maximum of about N = 4.5 according to PSE, indicating the amplitude ratio of the waves from seeding to the end of the cone should approach 90. Current results calculated by comparing pressure fluctuation levels between axial stations at a given time step indicate growth closer to N = 3 (amplitude ratio of 20.) The reasons for this are still under investigation. The current grid ($x^+ = z^+ \approx 15$) uses resolution somewhat coarser than what would be recommended by DNS best practices ($x^+ = z^+ \approx 5$) [26] and increased resolution possibly would improve the tracking of small fluctuations. With the current perturbation technique, the 2nd mode waves appear as random, non-homogenous packets, making the extraction of growth from a single solution time-step somewhat imprecise since each packet has a different initial amplitude. A more accurate measure of growth could be obtained by tracking a single wave packet over several time steps.

As can be seen in Figure 34, at $p_{rms} \approx 0.09\%$, all cases exhibit some level of 2nd mode growth, but insufficient to cause transition outside the wake. Within the wake, the k = 0.53 mm case does show some instability growth, but remains laminar. The case for k = 0.36 mm under these conditions was not calculated, but can reasonably be assumed to be laminar. Cases with k = 0.71 mm and k = 0.89 mm cases transition in the wake of the trip, but upstream of the computational location calculated for $p_{rms} \approx 0.00\%$. The direction of this movement is consistent with the observed experimental trends. Comparing the transition locations for this case, the computational transition location is downstream of the experimentally observed location for a given trip height under quiet flow. The experimental data reports pressure fluctuations as measured by a pitot probe placed into the freestream as $pitot_{rms} \approx 0.05\%$.

Increasing the added perturbations to $p_{rms} \approx 0.18\%$ causes transition to turbulence for all cases with k = 0.53 mm and larger while the case with k = 0.36 mm remains laminar. Instantaneous surface heating contours of these cases can be seen in Figure 35. With this level of perturbation, the transition locations relative to Re_{kk} match reasonably well with the experimental quiet wind tunnel data.

Increasing the added disturbances dramatically to $p_{rms} \approx 0.94\%$ produces the contours seen in Figure 10. For k = 0.36 mm, despite the strong level of perturbations, the wake of the trip remains laminar. Cases with k = 0.53 mm and k= 0.71 mm transition within the wake upstream of the locations measured under lower levels of perturbation. The area outside the wake remains laminar for all cases despite the high level of perturbation. For reference, experimental data suggests that conventional/noisy flow (reported level of $pitot_{rms} \approx 2.50\% - 3.50\%$) causes transition at 0.90 x/L of the cone outside the wake. This result suggests that this level of p_{rms} 0.94% remains less than what is experienced in a conventional/noisy facility.

Figure 38, Figure 39, and Figure 40 illustrate the time-averaged heat transfer coefficient for $p_{rms} = 0.09\%$, $p_{rms} = 0.18\%$ and $p_{rms} = 0.94\%$, respectively. These figures illustrate the roughness wake and the rise in mean heating levels associated with transition downstream of the roughness element. It should be noted that transition was defined in the computation as the first rise in heating at the y=0 location. The first images in each of Figure 38 through Figure 40 is transitional by this definition, but the initial transitional heating rise is not resolvable within the contour levels.

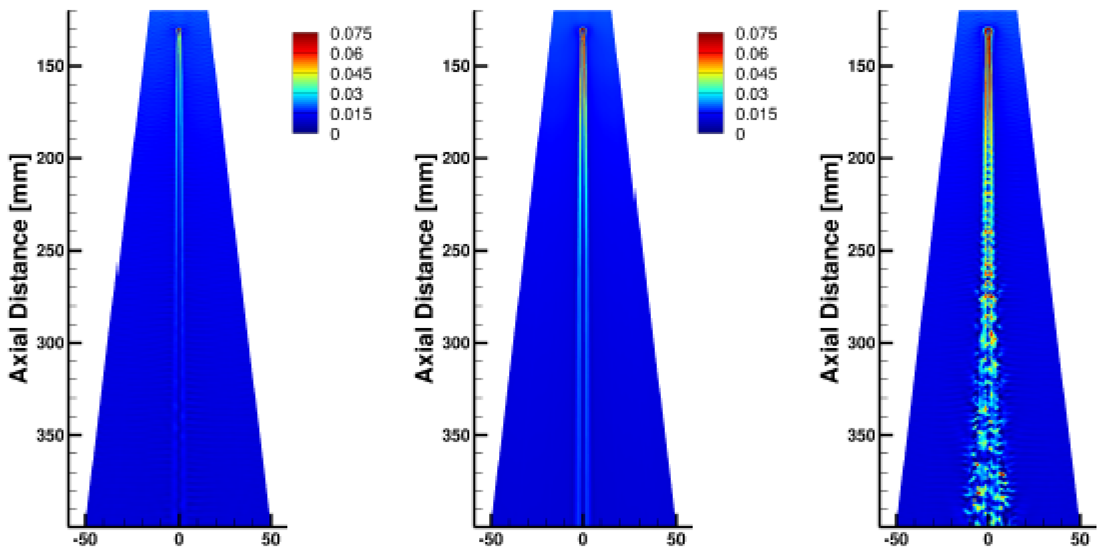

a) k = 0.53 mm b) k = 0.71 mm c) k = 0.89 mm

Figure 34 Instantaneous Surface Heating Coefficient, 0° AoA, $p_{rms} \approx 0.09\%$

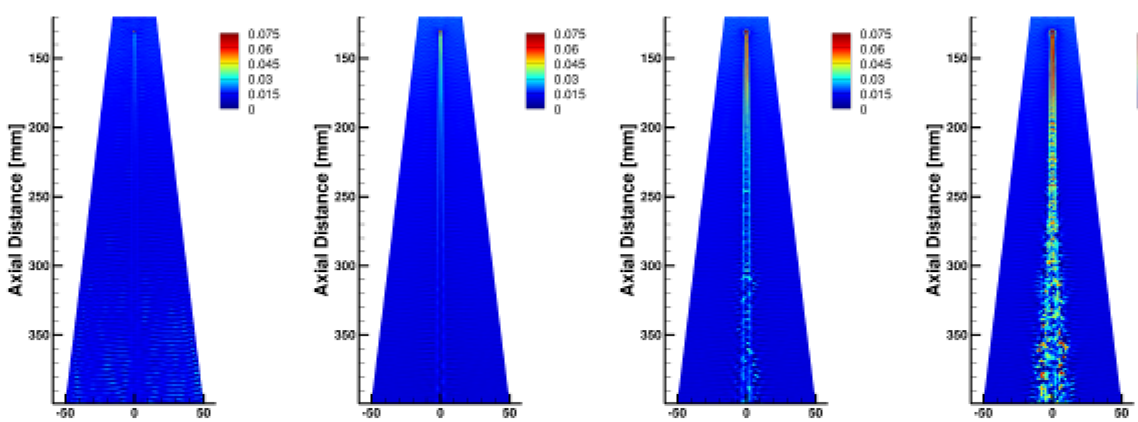

a) k = 0.36 mm b) k = 0.53 mm c) k = 0.71 mm d) k = 0.89 mm

Figure 35 Instantaneous Surface Heating Coefficient, 0° AoA, $p_{rms} \approx 0.18\%$

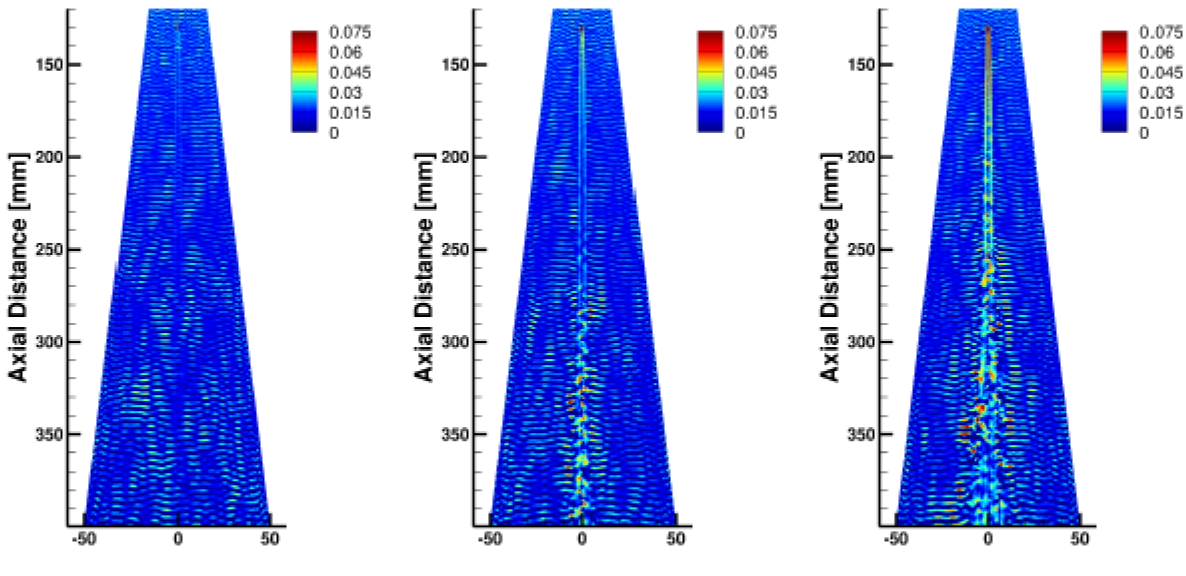

a) k = 0.36 mm b) k = 0.53 mm c) k = 0.71 mm

Figure 36 Instantaneous Surface Heating Coefficient, 0° AoA, $p_{rms} \approx 0.94\%$

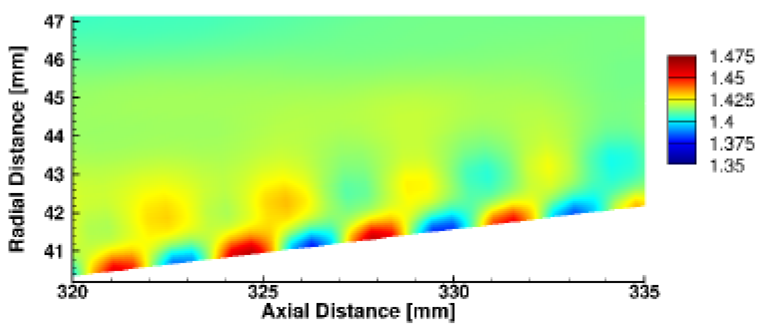

Figure 37 Streamwise Slice of p/p_∞, 0° AoA, k = 0.53 mm, $p_{rms} \approx 0.18\%$

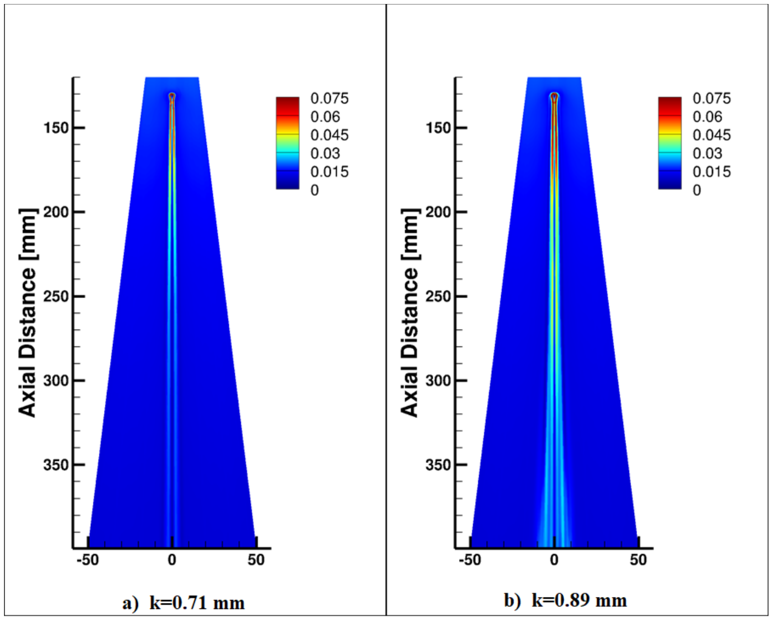

Figure 38 Time-averaged Surface Heating Coefficient, 0° AoA, prms ≈ 0.09%

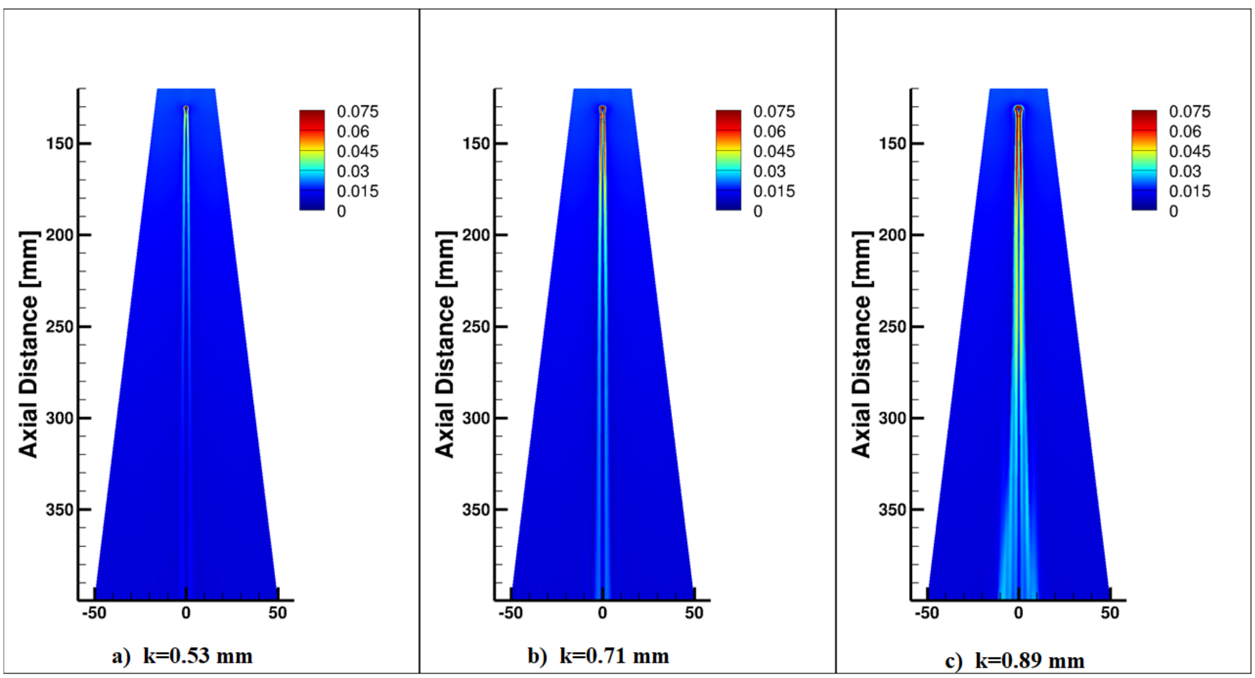

Figure 39 Time-averaged Surface Heating Coefficient, 0° AoA, p_{rms} ≈ 0.18%

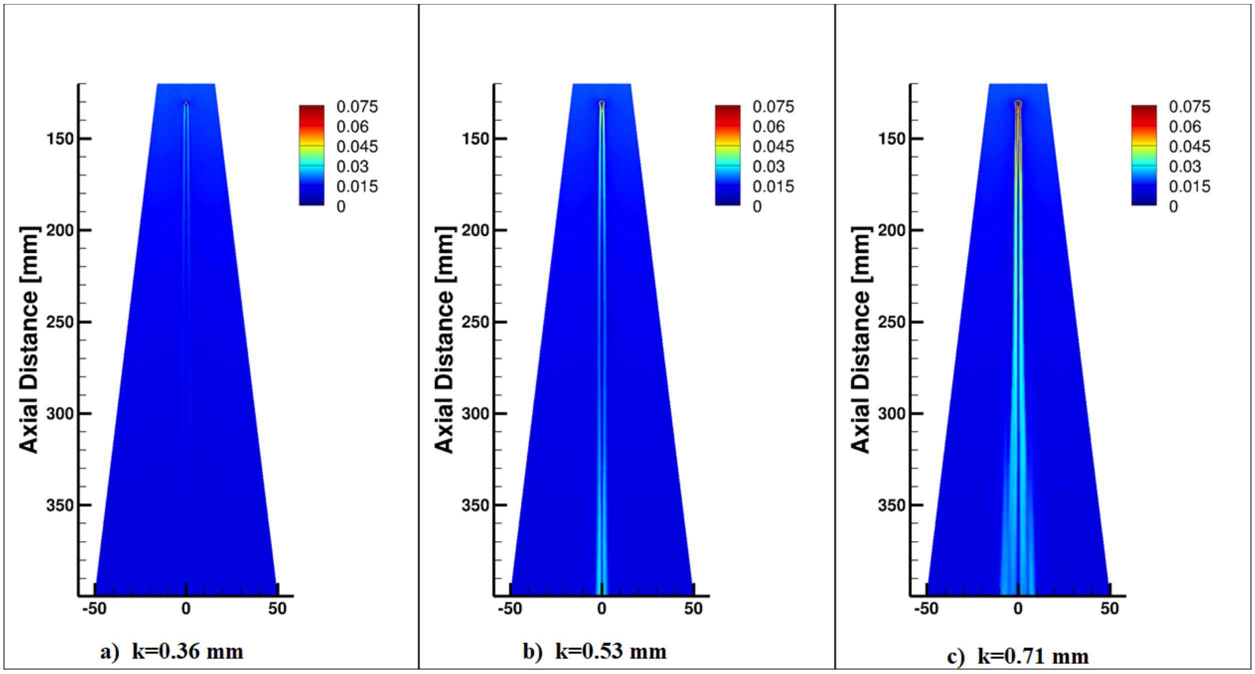

Figure 40 Time-averaged Surface Heating Coefficient, 0° AoA, p_{rms} ≈ 0.94%

Higher level of disturbances beyond about $p_{rms} \approx 1.25\%$ cannot be calculated with the current solver settings and grid system, as the solution became numerically unstable. Therefore replication of the noisy flow perturbation levels are not presented.

A combined line plot of transition location vs. Re_{kk} for all the computational turbulence levels calculated at 0° AoA can be seen in Figure 41. It can be seen in this plot that the addition of perturbations to the system improves the agreement with the experimental quiet flow data, and that the trend with increased disturbance levels is correct. The level of perturbations giving $p_{rms} \approx 0.18\%$ match the quiet experimental data the closest. Perturbations with $p_{rms} \approx 0.94\%$ as a trend transition upstream of the experimentally reported data; however, this is likely a higher level of fluctuations than were reported experimentally for quiet flow.

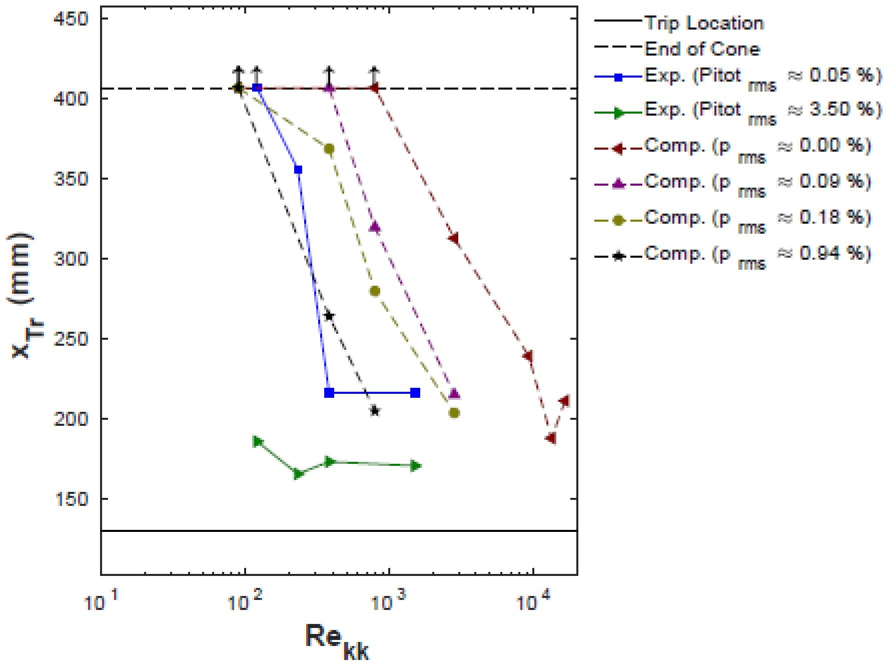

Figure 41 AoA Combined Transition Curves

3.5.2. 6° Angle of Attack

Cases were also calculated at 6° AoA with the trip located on the windward ray. At 6° AoA the flow reacts more dramatically to the perturbations than at 0° AoA. For a level of $p_{rms} \approx 1.11\%$ the entire circumference of the cone appears to undergo transition, as opposed to the 0° AoA cases which remain laminar outside the wake even at a similar $p_{rms} \approx 0.91\%$.

For $k = 0.53$ mm, transition as determined by heat flux reversal described above occurs within the wake approximately 200 mm from the nose for $p_{rms} \approx 0.10\%$ and approximately 165 mm for $p_{rms} \approx 1.11\%$, similar to the fully effective location reported experimentally. Top-down contours of instantaneous surface heating along the windward side can be seen in Figure 42.

Figure 43 and Figure 44 illustrate time-averaged surface heating contours for the windward ray for $p_{rms} \approx 0.1\%$ and $p_{rms} \approx 1.11\%$. Each figure contains heating contours for roughness heights of 0.36 and 0.53 mm.

Side-views of the contours of instantaneous surface heating can be seen in Figure 45. Note the traveling waves generated near the windward ray (bottom of figure) and convecting to the leeward side (top of the figure) and causing breakdown to small scales indicative of transition. The footprint of stationary crossflow vortices are visible in Figure 45a, note that the traveling waves visible in the $p_{rms} \approx 0.10\%$ and $p_{rms} \approx 1.11\%$ cases do not follow the same trajectory as the stationary crossflow vortices. The convection of these unsteady, traveling, waves therefore appears to be a separate process from secondary instability that might be expected in stationary crossflow waves. Outside the wake for both noisy cases, transition appears to occur earliest near the leeward ray, a result similar to the experimentally observed transition fronts.

A combined line plot of transition location vs. Re_{kk} for all the computational turbulence levels calculated at 6° AoA can be seen in Figure 46. Again, it can be seen in this plot that the addition of perturbations to the system improves the agreement with the experimental quiet flow data, and that the trend with increased disturbance levels is correct.

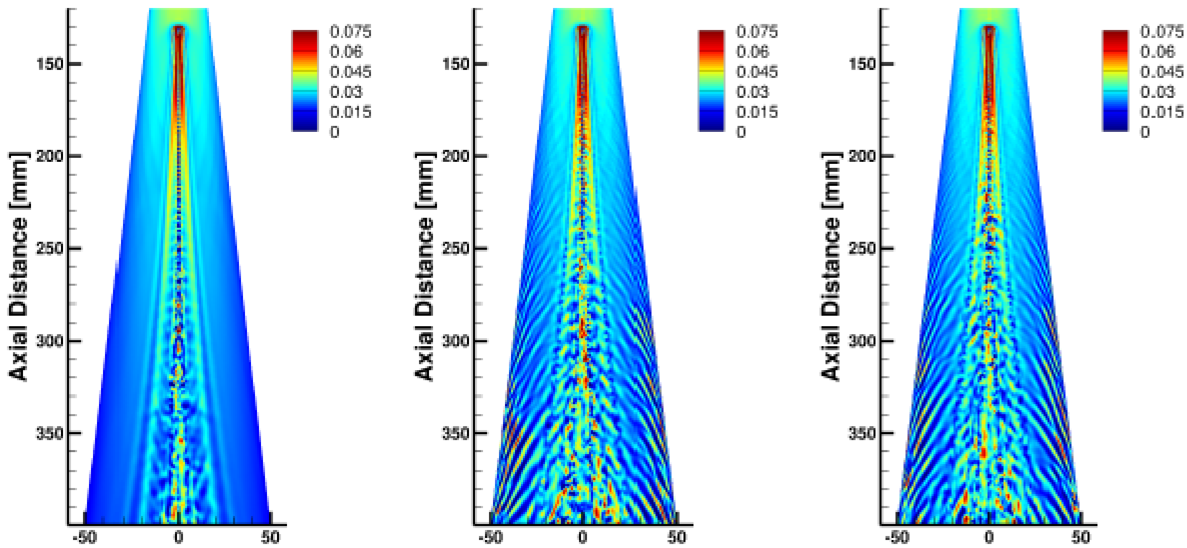

a) $p_{rms} \approx 0.00\%$ b) $p_{rms} \approx 0.10\%$ c) $p_{rms} \approx 1.11\%$

Figure 42 Instantaneous Surface Heating Coefficient, 6° AoA, Windward Ray, k = 0.53 mm

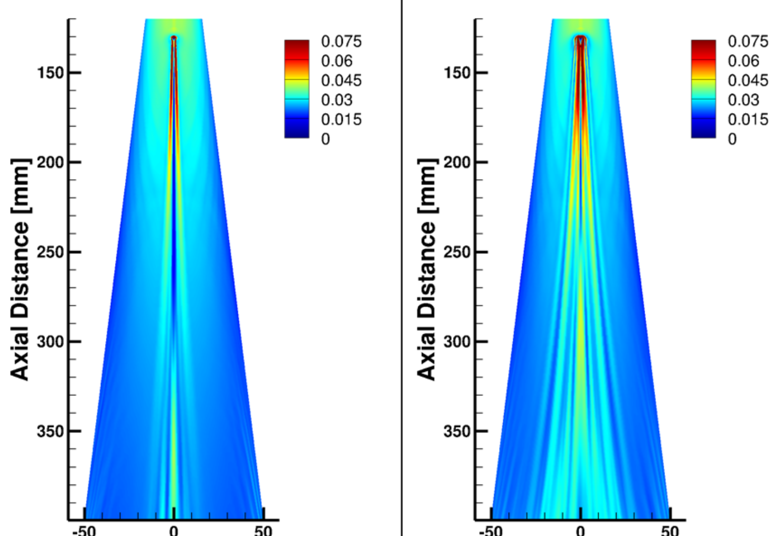

a) k=0.36 mm b) k=0.53 mm

Figure 43 Time-averaged Surface Heating Coefficient, 6° AoA, Windward Ray, $p_{rms} \approx$ 0.10%

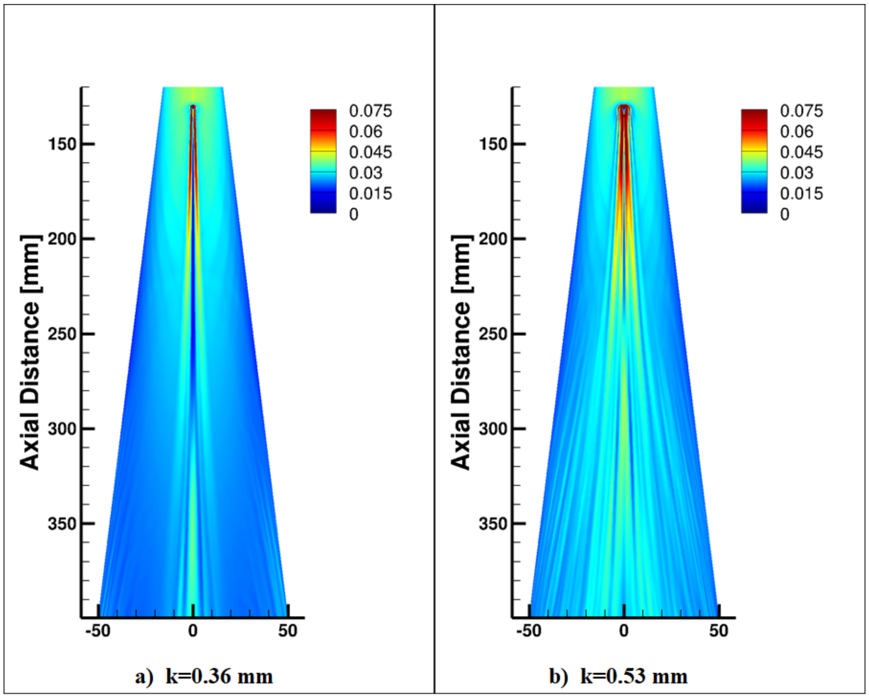

Figure 44 Time-averaged Surface Heating Coefficient, 6° AoA, Windward Ray, $p_{rms} \approx$ 1.11%

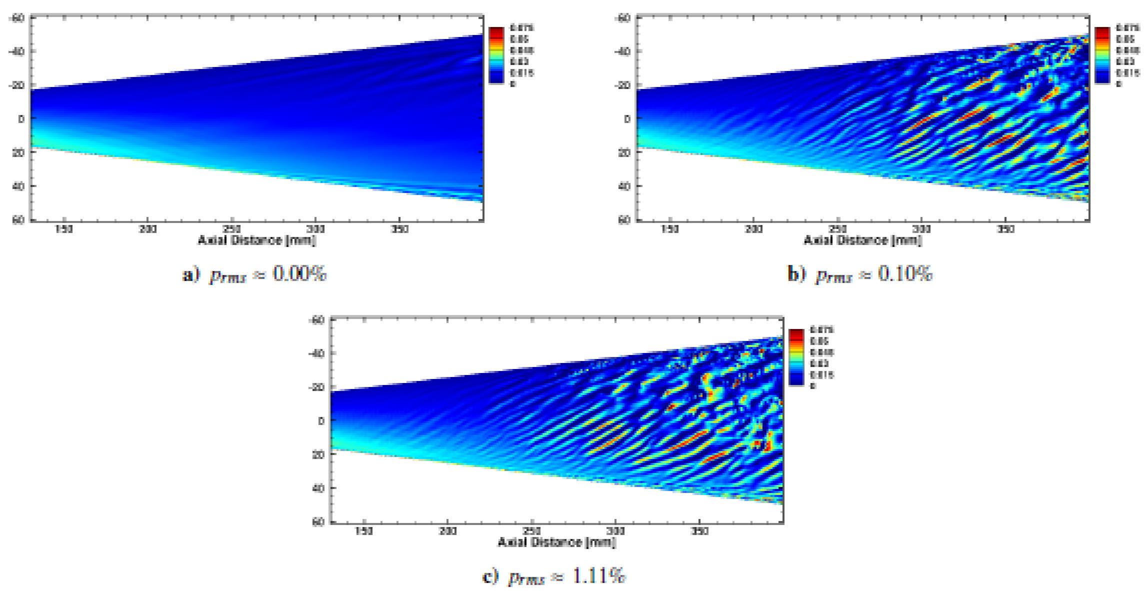

Figure 45 Instantaneous Surface Heating Coefficient, 6° AoA, k = 0.53 mm, Side View

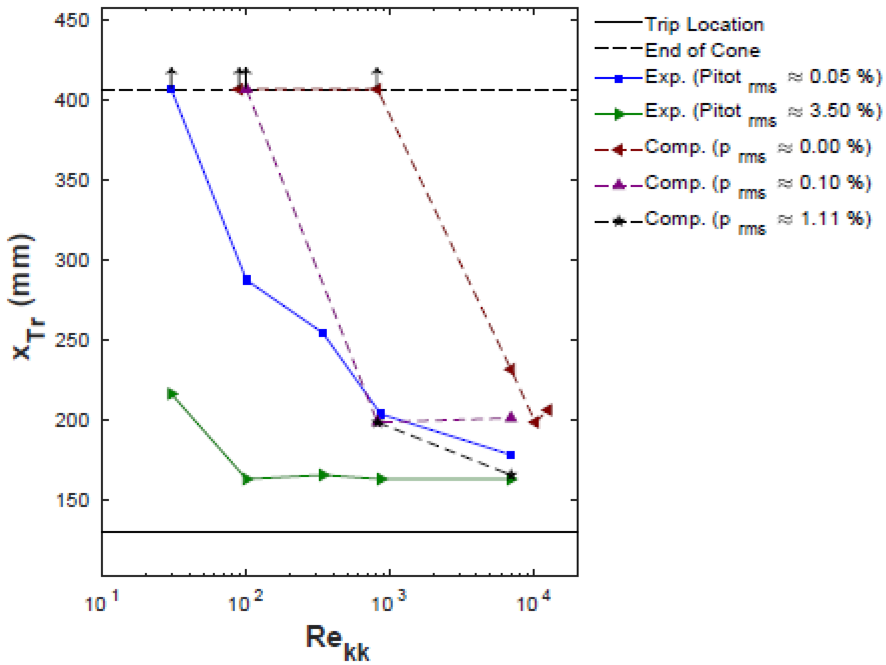

Figure 46 AoA Combined Transition Curves, Roughness Windward

3.6. Section 3 Conclusions

High-fidelity wall-resolved calculations have been performed for a hypersonic flowfield containing an isolated roughness element large enough to induce transition using a grid based on implicit large-eddy simulation resolution criteria. These calculations have been performed both with and without the addition of planar acoustic waves inserted near the wall, inside of the shock.

The computationally observed transition location was found to vary with level of added perturbation. With no perturbations added, transition occurs downstream of the experimentally observed location for a given trip height. For the current grid system and solver settings a $p_{rms} \approx$ 0.18% was required to approach the experimental transition locations. The change in transition location with the addition of added perturbations is in keeping with trends observed in experimental data.

The computational system contains numerical dissipation, and the computations also do not include vortical and entropy perturbation. Increased computational resolution and inclusion of all disturbance types present in the experiment would likely change the required level of fluctuations needed to match experimental data. However once a disturbance field has been "tuned" for a given resolution and numerical solution scheme, it is plausible to investigate parametric effects (e.g., the effect of trip height) on transition location with the implicit large-eddy simulation methodology. Assessing the effect of a complex flow field such as the wake of an isolated roughness element is difficult with standard techniques, such as the Parabolized Stability Equations, but appears to be feasible using implicit large-eddy simulation.

4. Conclusions and Future Work

The HIFiRE-5b flight test continues to shed light on boundary layer transition in hypersonic flight. This study showed that transition zone length on the HIFiRE-5b vehicle was generally shorter than the laminar length preceding it, although it was not as short as that observed for some supersonic quiet tunnel tests. [7] Analysis of transitional heating overshoot on the centerline, leading edge and 45° rays revealed that the leading edge and 45° rays had distinct overshoots above equilibrium turbulent heating levels. The centerline ray did not show a well-defined overshoot, but heating levels as analyzed on this ray also displayed a large amount of scatter, making overshoot somewhat difficult to discern. Turbulent spot generation rates inferred from flight data using spot generation models were consistent with rates inferred from ground measurements. Together, these results provide a modest foundation of flight data for anchoring transitional hypersonic boundary layer models.

Although the HIFiRE-5b flight data have been extensively exploited, some additional analysis would refine our understanding of the transitional region. With the transition zone length, overshoot and spot-generation rates defined, a logical next step would be to apply a Dhawan-Narasimha model [24] to determine if it is possible to tune the model parameters to the flight data in a consistent way. Also, the magnitude of the overshoot was determined in a somewhat ad-hoc manner with limited CFD data. Recomputed laminar and turbulent heating rates coupled to a 3D aeroshell conduction model would be useful in providing bounds on the overshoot magnitude.

In addition to the thermocouple-derived heating data, HIFiRE-5b obtained transitional data with Vatell heat-flux sensors and Kulite pressure transducers. It was demonstrated that these transducers give different transition onset locations and responses, due to their differing sensitivity [55]. Analysis of these data would provide additional bounds on the transitional zone length, as well as insight into pressure fluctuations.

An unanswered question from the transitional zone analysis is how the flight transition zone characteristics compare to ground data. Quiet tunnel data were too limited to make a good comparison. Noisy tunnel data suffered from several deficiencies. The most complete noisy tunnel data sets, those from the NASA Langley Mach 6 tunnel and the Purdue University quiet tunnel (run in conventional mode) were taken with Mach numbers and wall-to-stagnation-temperature ratios that were significantly different from flight. Data from Purdue University were somewhat limited and difficult to interpret. Tabulated data from the NASA Langley tests had been extracted in a Cartesian *x-y* grid, rather than along rays, which made them unsuitable for extracting data from the 45° ray. Some additional analysis of ground data may improve their utility.

In addition to mining of the existing HIFiRE-5 data, new analysis and experiments would be useful in understanding the transitional zone. The physics of heating overshoot remains murky. DNS simulations and experiment would be helpful in providing a more fundamental model of both the transitional zone and overshoot. Also, spot-generation rates could not be measured directly on HIFiRE-5b, due to the limited frequency-response of the Kulite pressure transducers. Higher frequency transducers, both in ground and flight test, might provide direct measurement of turbulent spots.

High-fidelity CFD, with acoustic disturbances simulated downstream of the shock, was shown to reproduce some transition trends with respect to wind tunnel noise and roughness. An attractive feature of this method is that the disturbance field may be simulated without having to fully resolve the difficult free stream noise/shock interaction. This allows more simulations to be performed, permitting parametric trends to be explored, as was reported in Section 3. Logical next steps would be to include vorticity and entropy disturbances and explore three-dimensional flow fields. These investigations are underway. If these results show promise, a further extension would be to try to calibrate the computational noise field to reproduce quantitative flight and wind tunnel transition data.

5. References

[1] Kimmel, R. L., Borg, M. P., Jewell, J. S., Miller, J. H. and Prabhu, D., "HIFiRE-5 Boundary Layer Transition And HIFiRE-1 Shock Boundary Layer Interaction," interim technical report AFRL-RQ-WP-TR-2015-0151, October 2015, Air Force Research Laboratory, Wright-Patterson Air Force Base, OH.

[2] Kimmel, R., Jewell, J. S., Borg, M. Hagen, B., Lam, B. and Parziale, N., "Hypersonic Boundary Layer Transition Experiments - Hypersonic International Flight Research Experimentation 5 (HIFiRE-5) and Circular Cone," interim technical report AFRL-RQ-WP-TR-2017-0098, October 2016, Air Force Research Laboratory, Wright-Patterson Air Force Base, OH.

[3] Kimmel, R., Adamczak, D., Borg, M., Jewell, J. S., Juliano, T. J., Tufts, M., "Transition On Hypersonic Vehicles With Crossflow," interim technical report AFRL-RQ-WP-TR-2017-0149, November 2017, Air Force Research Laboratory, Wright-Patterson Air Force Base, OH.

[4] Kimmel, R., Adamczak, Borg, M., Jewell, J. S., Tufts, M., Kennedy, R. and Laurence, S., "Blunt Cone, HIFiRE-1 and HIFiRE-5 Boundary Layer Transition," interim technical report AFRL-RQ-WP-TR-2018-0161, July 2018, Air Force Research Laboratory, Wright-Patterson Air Force Base, OH.

[5] Juliano, T. J., Jewell, J. S. and Kimmel, R. L., "HIFiRE-5b Boundary-Layer Transition Length and Turbulent Overshoot," AIAA paper 2019-2970, June 2019. DOI: 0.2514/6.2019-2970

[6] Tufts, M. W., Bisek, N. J. and Kimmel, R. L., "Implicit Large-Eddy Simulation of Discrete Roughness Boundary-Layer Transition with Added Perturbations," AIAA paper 2019-2967, June 2019. DOI: 10.2514/6.2019-2967

[7] Chen, F.-J., "Boundary-Layer Transition Extent Measurements on a Cone and Flat Plate at Mach 3.5," AIAA paper 1993-0342, January 1993.

[8] Kimmel, R. L., Adamczak, D. W., Hartley, D., Alesi, H., Frost, M. A., Pietsch, R., Shannon, J., and Silvester, T., "Hypersonic International Flight Research Experimentation-5b Flight Overview," *Journal of Spacecraft and Rockets*, Vol. 55, No. 6, 2018, pp. 1303–1314. doi:10.2514/1.A34148

[9] Kimmel, R. L., Adamczak, D., Juliano, T. J., and the DSTO AVD Brisbane Team, "HIFiRE-5 Flight Test Preliminary Results," AIAA Paper 2013-0377, January 2013.

[10] Jewell, J. S., Kimmel, R. L., Adamczak, D. W., Poggie, J., Porter, K. M., and Juliano, T. J., "HIFiRE-5b Flow Computations and Attitude Determination via Comparison with Flight Data," Journal of Spacecraft and Rockets, Vol. 55, No. 6, 2018, pp. 1356–1368. doi:10.2514/1.A34162.

[11] Jewell, J. S., Miller, J. H., and Kimmel, R. L., "Correlation of HIFiRE-5a Flight Data With Computed Pressure and Heat Transfer," Journal of Spacecraft and Rockets, Vol. 54, No. 5, 2017, pp. 1142–1152.

[12] Borg, M. P., and Kimmel, R. L., "Ground Test Measurements of Boundary-Layer Instabilities and Transition for HIFiRE-5 at Flight-Relevant Attitudes," Journal of Spacecraft and Rockets, vol. 55, no. 6, 2018, pp. 1329–1340. doi:10.2514/1.A34163.

[13] Juliano, T. J., Poggie, J., Porter, K. M., Kimmel, R. L., Jewell, J. S., and Adamczak, D. W., "HIFiRE-5b Heat Flux and Boundary-Layer Transition," Journal of Spacecraft and Rockets, Vol. 55, No. 6, 2018, pp. 1315–1328. doi:10.2514/1.A34147.

[14] Juliano, T. J., Jewell, J. S., and Kimmel, R. L., "HIFiRE-5b Boundary-Layer Transition — With Attitude," AIAA Paper 2018-2891, June 2018.

[15] Juliano, T. J., Jewell, J. S. and Kimmel, R. L., "Effects of Attitude on HIFiRE-5b Boundary-Layer Transition," AIAA Journal of Spacecraft and Rockets, vol. 56, no. 4, July-August 2019, pp. 1045-1059. DOI: 10.2514/1.A34352

[16] Kimmel, R. L., and Adamczak, D., "HIFiRE-1 Background and Lessons Learned," AIAA Paper 2012-1088, January 2012.

[17] Boyd, C. F., and Howell, A., "Numerical Investigation of One-Dimensional Heat-Flux Calculations," Tech. Rep. NSWCDD/TR-94/114, Dahlgren Division Naval Surface Warfare Center, Silver Spring, MD 20903-5640, October 1994.

[18] Anderson Jr., J. D., Hypersonic and High Temperature Gas Dynamics, 2nd ed., American Institute of Aeronautics and Astronautics, Inc., Reston, VA, 2000, Chaps. 6, Viscous Flow: Basic Aspects, Boundary Layer Results, and Aerodynamic Heating, pp. 213–300.

[19] Parks, T. W., and McClellan, J. H., "Chebyshev Approximation for Nonrecursive Digital Filters with Linear Phase," IEEE Transactions on Circuit Theory, Vol. CT-19, No. 2, 1972, pp. 189–194.

[20] Juliano, T. J., Poggie, J., Porter, K. M., Kimmel, R. L., Jewell, J. S., and Adamczak, D. W., "HIFiRE-5b Heat Flux and Boundary-Layer Transition," AIAA Paper 2017-3134, June 2017. doi:10.2514/6.2017-3134.

[21] Jewell, J. S., Leyva, I. A., and Shepherd, J. E., "Turbulent spots in hypervelocity flow," Experiments in Fluids, Vol. 58, No. 32, 2017. doi:10.1007/s00348-017-2317-y.

[22] Mee, D. J., and Tanguy, G., "Turbulent Spot Initiation Rates in Boundary Layers in a Shock Tunnel," Proceedings of the 29th International Symposium on Shock Waves, ISSW29-000194, Madison, WI, 2013, pp. 623–628. doi:10/bf8b.

[23] Narasimha, R., "On the distribution of intermittency in the transition region of a boundary layer," Journal of the Aeronautical Sciences, Vol. 24, No. 9, 1957, pp. 711–712. doi:10.2514/8.3944.

[24] Narasimha, R., "The Laminar-Turbulent Transition Zone in the Boundary Layer," Progress in Aerospace Sciences, Vol. 22, 1985, pp. 29–80. doi:10.1016/0376-0421(85)90004-1.

[25] Cebeci, T., and Smith, A. M. O., Analysis of turbulent boundary layers, Academic Press, London, 1974.

[26] Emmons, H. W., "The laminar-turbulent transition in a boundary layer: Part I," Journal of the Aeronautical Sciences, Vol. 18, No. 7, 1951. doi:10.2514/8.2010.

[27] Vinod, N., and Rama, G., "Pattern of breakdown of laminar flow into turbulent spots," Physical Review Letters, Vol. 93, No. 11, 2004, pp. 114501–1–4. doi:10.1103/PhysRevLett.93.114501

[28] Doorley, D. J., and Smith, F. T., "Initial-value problems for spot disturbances in incompressible or compressible boundary layers," Journal of Engineering Mathematics, Vol. 26, No. 1, 1992, pp. 87–106. doi:10.1007/BF00043229.

[29] Anderson, J. D., Hypersonic and High-Temperature Gas Dynamics, Second Edition, American Institute of Aeronautics and Astronautics, 1801 Alexander Bell Drive, Reston, Virginia 20191, 2006, pp. 335.

[30] Morkovin, M. V., Reshotko, E., and Herbert, T., "Transition in open flow systems-a reassessment," Bull. Am. Phys. Soc, Vol. 39, No. 9, 1994, pp. 1882.

[31] Tufts, M. W., Gosse, R. C., and Kimmel, R. L., "PSE Analysis of Crossflow Instability on HIFiRE 5b Flight," AIAA-2017-3136, 2017.

[32] Van Ingen, J. L., "A Suggested Semi-Empirical Method for the Calculation of the Boundary Layer Transition Region," Dept. Aero. Eng., Inst. of Technology Delft, Report V.T.H. 74, 1956.

[33] Reed, H. L., Reshotko, E., and Saric, W. S., "Receptivity: The Inspiration of Mark Morkovin," AIAA-2015-2471, 2015.

[34] Malik, M. R., Lin, R. S., and R., S., "Computation of Hypersonic Boundary-Layer Response to External Disturbances," AIAA-1999-0411, 1999.

[35] Ma, Y. and Zhong, X., "Receptivity to Freestream Disturbances of Mach 8 Flow over a Sharp Wedge," AIAA-2003-0788, 2003.

[36] Malik, M. R., Lin, R. S., and R., S., "Computation of Hypersonic Boundary-Layer Response to External Disturbances," AIAA-1999-0411, 1999.

[37] Wang, X., Zhong, X., and Ma, Y., "Response of a Hypersonic Boundary Layer to Wall Blowing–Suction," AIAA Journal, Vol. 49, No. 7, 2011, pp. 1336–1353.

[38] Balakumar, P., "Transition in a Supersonic Boundary-Layer Due to Roughness and Acoustic Disturbances," AIAA-2003-3589, 2003.

[39] Fong, K. D., Wang, X., Huang, Y., Zhong, X., McKiernan, G. R., Fisher, R. A., and Schneider, S. P., "Second Mode Suppression in Hypersonic Boundary Layer by Roughness: Design and Experiments," AIAA Journal, Vol. 53, No. 10, 2015, pp. 3138–3143.

[40] Fong, K. D., Wang, X., and Zhong, X., "Stabilization of Hypersonic Boundary Layer by 2-D Surface Roughness," AIAA-2015-2985, 2015.

[41] Gronvall, J. E., Johnson, H. B., and Candler, G. V., "Hypersonic Three-Dimensional Boundary Layer Transition on a Cone at Angle of Attack," AIAA-2011-3561, 2011.

[42] Gronvall, J. E., Johnson, H. B., and Candler, G. V., "Hypersonic Three-Dimensional Boundary Layer Transition on a Cone at Angle of Attack," AIAA-2012-2822, 2012.

[43] Gronvall, J. E., Bisek, N. J., and Poggie, J., "High Fidelity Computational Study of the HIFiRE-1 Boundary Layer Trip,"AIAA-2014-0433, 2014.

[44] Hader, C. and Fasel, H., "Towards Simulating Natural Transition in Hypersonic Boundary Layers via Random Inflow Disturbances," Journal of Fluid Mechanics, Vol. 847, No. R3, 2018, pp. 1–14, doi:10.1017/jfm/2018.386.

[45] Hader, C. and Fasel, H., "Direct Numerical Simulations of Hypersonic Boundary-Layer Transition for a Flared Cone: Fundamental Breakdown," Journal of Fluid Mechanics, Vol. 869, 2019, pp. 1341–384, doi:10.1017/jfm/2019.202.

[46] Saric,W. S.,West, D. E., Tufts, M.W., and Reed, H. L., "Flight Test Experiments on Discrete Roughness Element Technology for Laminar Flow Control," AIAA-2015-0539, 2015.

[47] Tufts, M. W., Bisek, N. J., Kimmel, R. L., and Mallinak, R., "Computational Investigation of Effective Trip Heights in Hypersonic Flows," AIAA-2019-0875, 2019.

[48] Casper, K. M., Johnson, H. B., and Schneider, S. P., "Effect of Freestream Noise on Roughness-Induced Transition for a Slender Cone," Journal of Spacecraft and Rockets, Vol. 48, No. 3, 2011, pp. 406–413.

[49] Jespersen, D., Pulliam, T., and Buning, P. G., "Recent Enhancements to OVERFLOW," AIAA-97-0644, 1997.

[50] Suhs, N. E., Rogers, S. E., and Dietz, W. E., "Pegasus 5: An Automated Pre-Processor for Overset-Grid CFD," AIAA-2002-3186, 2002.

[51] Cerminara, A., Durant, A., Andr´e, T., Sandham, N. D., and Taylor, N. J., "DNS of Acoustic Receptivity and Breakdown in a Mach 6 Flow over a Generic Forebody," AIAA-2018-0348, 2018.

[52] Chaudhry, R. S. and Candler, G. V., "Computing Measured Spectra from Hypersonic Pitot Probes with Flow-Parallel Freestream Disturbances," AIAA Journal, Vol. 55, No. 12, 2017, pp. 4155–4166.

[53] Chaudhry, R. S., Candler, G. V., Gray, K. A., and Schneider, S. P., "Computations of Measured Pitot-Probe Spectra using Angled Freestream Disturbances and Comparisons to Experiments," AIAA-2019-2149, 2019.

[54] Fedorov, A. V., "Receptivity of High Speed Boundary Layer to Acoustic Disturbances," AIAA-2002-2846, 2002.

[55] Kimmel, R. L., Adamczak, D. A., and DSTG AVD Brisbane Team, "HIFiRE-5b Flight Overview," AIAA paper 2017-3131, June 2017. DOI: 10.2514/6.2017-3131

List of Acronyms, Abbreviations, Symbols

a = sound speed, m/s
c = turbulent spot convection speed, m/s
c_h = heat transfer coefficient, dimensionless
c_p = specific heat, J/kg/K
f = frequency, units as noted
k = roughness height or wave number, units as noted
M = Mach number, dimensionless
N = dimensionless disturbance amplitude, $\ln(A/A_0)$, where A_0 is amplitude at lower neutral bound
n = spot generation parameter
p = pressure, Pa
$\bar{p}$ = averaged pressure
$\dot{q}''$ = heat transfer rate, W/m^2
R = correlation coefficient, dimensionless
Re = freestream unit Reynolds number, per meter
Re_{kk} = Reynolds number based on roughness height and flow conditions at top of roughness element, dimensionless
Re_x = Reynolds number based on freestream (upstream of bow shock) conditions and axial length
St = Stanton number, dimensionless
T = temperature, K
t = time, seconds
u,v,w = velocity, m/s
x,y,z = spatial coordinates, units as noted
α = angle-of-attack, degrees
β = yaw angle, degrees
ε = perturbation amplitude parameter
γ = intermittency or ratio of specific heats, as noted
ϕ = azimuthal coordinate in body-fixed coordinate system, degrees; or phase angle, radians
ρ = density, kg/m^3
σ = standard deviation, units as noted; or turbulent spot growth parameter
μ = viscosity
ω = wave frequency

Superscripts
$'$ = perturbation
$+$ = wall coordinates

Subscripts
end = end of transition
fit = derived from empirical fit
flight = measured in flight
i,j,k = index number
le = leading edge
onset = transition onset
rms = root mean square
te = trailing edge

Tr = transition
w = wall
0 = stagnation conditions
∞ = free stream, upstream of model bow shock

Acronyms

AC	alternating current
AoA	angle of attack
BAM6QT	Boeing/AFOSR Mach 6 Quiet Tunnel
BOLT	boundary layer transition
CFD	computational fluid dynamics
DC	direct current
GPS	global positioning system
HIFiRE	Hypersonic International Flight Research Experiments
HLLC	Harten-Lax-van-Leer contact
IMU	inertial measurement unit
NASA	National Aeronautics and Space Administration
PSE	parabolized stability equation
SSOR	symmetric successive over-relaxation
WENO	weighted essentially non-oscillatory